

North Atlantic Response to Observed North Atlantic Oscillation Surface Heat Flux in Three Climate Models[©]

WHO M. KIM^{©,a} YOHAN RUPRICH-ROBERT,^b ALCIDE ZHAO,^c STEPHEN YEAGER,^a AND JON ROBSON^c

^a National Science Foundation, National Center for Atmospheric Research, Boulder, Colorado

^b Barcelona Supercomputing Center, Barcelona, Spain

^c National Centre for Atmospheric Science, University of Reading, Reading, United Kingdom

(Manuscript received 8 June 2023, in final form 18 November 2023, accepted 22 December 2023)

ABSTRACT: We investigate how the ocean responds to 10-yr persistent surface heat flux forcing over the subpolar North Atlantic (SPNA) associated with the observed winter NAO in three CMIP6-class coupled models. The experiments reveal a broadly consistent ocean response to the imposed NAO forcing. Positive NAO forcing produces anomalously dense water masses in the SPNA, increasing the southward lower (denser) limb of the Atlantic meridional overturning circulation (AMOC) in density coordinates. The southward propagation of the anomalous dense water generates a zonal pressure gradient overlying the models' North Atlantic Current that enhances the upper (lighter) limb of the density-space AMOC, increasing the heat and salt transport into the SPNA. However, the amplitude of the thermohaline process response differs substantially between the models. Intriguingly, the anomalous dense-water formation is not primarily driven directly by the imposed flux anomalies, but rather dominated by changes in isopycnal outcropping area and associated changes in surface water mass transformation (WMT) due to the background surface heat fluxes. The forcing initially alters the outcropping area in dense-water formation regions, but WMT due to the background surface heat fluxes through anomalous outcropping area decisively controls the total dense-water formation response and can explain the intermodel amplitude difference. Our study suggests that coupled models can simulate consistent mechanisms and spatial patterns of decadal SPNA variability when forced with the same anomalous buoyancy fluxes, but the amplitude of the response depends on the background states of the models.

KEYWORDS: North Atlantic Ocean; Decadal variability; North Atlantic Oscillation; Meridional overturning circulation

1. Introduction

The subpolar North Atlantic (SPNA) is an intriguing region as various processes induce fluctuations in upper-ocean properties on broad time scales with significant implications for climate (Chafik et al. 2016; Zhang et al. 2019). Lying directly below the energetic North Atlantic jet stream, the SPNA exhibits SST variability on a wide spectrum of time scales due to turbulent heat exchanges and Ekman transport associated with the jet's fluctuations (Visbeck et al. 2003; Deser et al. 2010). In the western basin and along its northern periphery, weak stratification and harsh winter conditions allow for deep and intermediate water formation, promoting vertical mixing of heat, salt, and trace gases (e.g., CO₂; Marshall and Schott 1999; Rhein et al. 2017). Observed SPNA SST also exhibits strong variability on decadal to multidecadal (simply decadal hereafter) time scales, as a part of the variability in the wider North Atlantic, often called Atlantic multidecadal variability (AMV; Kerr 2000). This decadal temperature variability in the SPNA is widely believed to be primarily generated by anomalous heat transport convergence due to ocean dynamics (Robson et al. 2012; Zhang et al. 2016; Moat et al. 2019; Kim

et al. 2020), particularly by the buoyancy-driven components of the Atlantic meridional overturning circulation (AMOC) and subpolar gyre circulation (Yeager 2020).

Mechanisms of decadal upper-ocean temperature (UOT) variability in the SPNA are of particular interest for the decadal prediction research community, given high decadal predictability consistently found from initialized hindcasts (Kirtman et al. 2013; Robson et al. 2014; Yeager and Robson 2017; Robson et al. 2018; Smith et al. 2019; Borchert et al. 2019; Yeager 2020). Decadal SPNA SST variability is often related to variations in surface temperature and precipitation in the surrounding continents on these time scales (Årthun et al. 2017; Simpson et al. 2019; Kim et al. 2020), including impactful extreme events (e.g., heat waves; Borchert et al. 2019; Qasmi et al. 2021). It is also ascribed as a source of decadal climate variability in remote regions, including Arctic sea ice extent in the Atlantic sector (Årthun et al. 2017; Yeager et al. 2015), Sahel precipitation (Dunstone et al. 2011; Kim et al. 2020), and hurricane activity (Smith et al. 2010; Dunstone et al. 2011; Kim et al. 2020). Therefore, improving predictions of how the SPNA will evolve (based on solid mechanistic understanding) will have many important implications. However, despite a long history of research, the mechanisms of decadal SPNA SST variability remain an active area of research and debate (Clement et al. 2015; Zhang et al. 2016; O'Reilly et al. 2016; Robson et al. 2016; Kim et al. 2018b; Josey et al. 2018; Oltmanns et al. 2020).

The leading hypothesis to explain decadal SPNA variability is a mechanistic link between anomalous surface buoyancy

[©] Supplemental information related to this paper is available at the Journals Online website: <https://doi.org/10.1175/JCLI-D-23-0301.s1>.

Corresponding author: Who M. Kim, whokim@ucar.edu

fluxes associated with the NAO during boreal winter, anomalous dense-water formation in the SPNA, and subsequent AMOC adjustment (Eden and Willebrand 2001; Robson et al. 2012; Yeager and Danabasoglu 2014; Yeager 2020; Kim et al. 2020). A strong AMOC enhances the northward heat and salt transport into the SPNA from the subtropics, resulting in upper-ocean heat and salt content gain in the SPNA, whereas a weaker AMOC does the opposite. The NAO can also directly generate SST variability through changes in the strength of the westerlies on decadal time scales (Deser et al. 2010; Clement et al. 2015; Barrier et al. 2015). However, model simulations suggest that this direct atmospheric-driven SST anomaly is overwhelmed by a delayed change in ocean heat transport (Lohmann et al. 2009; Delworth et al. 2017). Consistent with this, the decadal SPNA temperature variability lags the NAO by about a decade in observations (Kim et al. 2018a; Kim et al. 2023), implying that the dominant influence of NAO on decadal SPNA SST variability involves an ocean circulation change.

The impact of NAO-related buoyancy forcing on the ocean has been extensively investigated using numerical simulations. When forced with either observation-based surface forcing or idealized NAO forcing, ocean-only model simulations appear to show a robust response of the aforementioned mechanistic link (Eden and Willebrand 2001; Böning et al. 2006; Biastoch et al. 2008; Lohmann et al. 2009; Robson et al. 2012; Yeager and Danabasoglu 2014; Polo et al. 2014). Systematic comparisons across multiple models forced with the same forcing based on an atmospheric reanalysis reveal a consistent statistical relationship between the NAO and AMOC at subpolar latitudes (Danabasoglu et al. 2016; Xu et al. 2019), suggesting that when the NAO is realistic, the proposed oceanic mechanism seems to be at work in most models.

In coupled models, by contrast, the NAO-AMOC link is generally weaker and less robust across models (Ba et al. 2014; Xu et al. 2019; Kim et al. 2023). Xu et al. (2019) compare the statistical relationship between the NAO and AMOC from both forced ocean and coupled configurations that use the same ocean component. They show that in coupled configurations, the relationship is less robust while the same ocean models exhibit a more robust relationship when the models are forced with observed forcing. Many factors can contribute to this weak linkage in coupled models. For example, AMOC variability appears to be more sensitive in some models to freshwater flux from the Arctic Ocean rather than local surface buoyancy fluxes in deep-water formation regions (e.g., Jungclaus et al. 2005; Frankcombe et al. 2010; Lai et al. 2022). Different background states in the ocean can also change the efficacy of NAO-related buoyancy forcing for driving AMOC variability. Kim et al. (2023) show using preindustrial control simulations from CMIP6 that the strength of the NAO-AMOC relationship is significantly correlated with the mean SPNA stratification across the models, which is in turn related to sea ice extent in the SPNA that can prevent heat loss from the ocean.

The diversity of NAO-related surface buoyancy fluxes in coupled models is another factor that could contribute to the wide range of simulated connections between the NAO and

decadal SPNA variability. Even if the pattern of the NAO based on SLP is reasonable in coupled models (Wang et al. 2017; Fasullo et al. 2020), the associated buoyancy fluxes may not necessarily be realistic. Turbulent surface heat fluxes, the dominant component of NAO-related surface buoyancy fluxes, in the western SPNA are strongly controlled by air temperature (Kim et al. 2016), which is in turn controlled by the strength of westerlies, carrying cold air from the Canadian Arctic, that are enhanced during positive NAO. Therefore, an air temperature bias in these upstream regions or a displacement of the meridional pressure gradient can degrade the realism of simulated heat fluxes in the western SPNA. Also, it has been shown that simulated NAO in coupled models exhibits weaker decadal variability than observed (Wang et al. 2017; Kim et al. 2018a; Simpson et al. 2018). Given the importance of persistent SPNA buoyancy forcing in spinning up AMOC (Delworth and Zeng 2016; Kim et al. 2020; MacGilchrist et al. 2021), the weak decadal NAO variability simulated in models could also contribute to the weak connection.

To better understand the diverse NAO-AMOC relationship in coupled models, in this study, we impose surface heat flux forcing associated with the observed winter NAO over the SPNA for 10 years consistently in three CMIP6-class coupled models. By constraining the strength and duration of the NAO-related surface heat flux forcing based on observations, we can remove differences related to the realism of the NAO-related heat flux anomalies and focus on differences in the response to the identical NAO forcing, such as those arising from different background states. These numerical experiments are similar to those performed by previous studies (Delworth and Zeng 2016; Delworth et al. 2016, 2017; Kim et al. 2020). Delworth and colleagues apply observation-based NAO-related surface heat flux over the North Atlantic in GFDL coupled models in a series of studies and show that the NAO forcing induces expected AMOC and North Atlantic responses with far-reaching climate impacts (Delworth and Zeng 2016; Delworth et al. 2016, 2017). Kim et al. (2020) impose the same NAO surface heat flux forcing in the CESM1, but only in the Labrador Sea (LS) to perturb water-mass formation there and examine how the rest of the ocean and climate respond to this perturbation. They find many of the previously reported ocean and climate responses (e.g., changes in AMOC, SPNA UOT, and European surface climate) that are thought to be related to AMV. However, this protocol/approach has not been applied consistently in a multimodel framework to explore the response systematically to the observed NAO surface buoyancy forcing on decadal time scales under different mean background states.

To examine the relationship of the imposed forcing to AMOC changes, we adopt the widely used water mass transformation (WMT) analysis framework (e.g., Walin 1982; Speer and Tziperman 1992; Grist et al. 2014; Petit et al. 2021; Yeager et al. 2021) that estimates the volume flux of waters transformed from one density-class to another by surface buoyancy fluxes. Previous studies have shown that surface WMT reasonably captures the mean and decadal variability of AMOC in density coordinates (Grist et al. 2009; Josey et al. 2009).

In the next section (section 2), we briefly introduce the three coupled models used in the present study, describe the experimental design, and explain how WMT is calculated in practice. In section 3, we present the results of the study. Starting with a brief description of the background state of key variables in each model (section 3a), we present the responses of surface density fluxes (section 3b), WMT (section 3c), and AMOC (section 3d), followed by wider climate impacts (section 3e). The salient findings of the study are highlighted in section 4 with some concluding remarks.

2. Experimental design and methods

a. Models

CESM2 is the latest version of CESM used for CMIP6 simulations (Danabasoglu et al. 2020). CESM2 consists of POP2, CAM6, CICE5, and CLM5 for the ocean, atmosphere, sea ice, and land components, respectively, with a nominal 1° horizontal resolution for all components. Here, we briefly describe a few fundamental features of POP2 since the present study mostly focuses on the ocean. We refer to Danabasoglu et al. (2020) and references therein for a detailed description for each component model that includes updated features from CESM1. POP2 (as well as CICE5) uses a dipole grid with the North Pole displaced over Greenland, allowing for higher horizontal resolution around Greenland (30–50 km). The horizontal resolution also increases to 0.27° near the equator. It has 60 vertical levels with layer thickness monotonically increasing from 10 m in the upper ocean to 250 m in the deep ocean. POP2 exchanges fluxes with CAM6 and CICE5, calculated using the bulk formulas described in Large and Yeager (2009).

EC-Earth3P (Haarsma et al. 2020) is a coupled climate model consisting of an atmospheric component based on the cycle 36r4 of the Integrated Forecast System (IFS) atmosphere–land–wave model of ECMWF coupled to NEMO (v3.6). The H-TESSEL model is used for the land surface and is an integral part of IFS: for more details see Hazeleger and Bintanja (2012). The atmosphere and ocean/sea ice components are coupled through the OASIS coupler. The ice model, embedded in NEMO, is the Louvain la Neuve sea ice model version 3 (LIM3), which is a dynamic-thermodynamic sea ice model with five thickness categories. EC-Earth3P uses a reduced Gaussian-grid with 91 vertical levels and a T255 horizontal truncation/N128 grid resolution (~ 100 km) for the IFS atmosphere. The NEMO ocean has 75 vertical levels and a horizontal resolution of about 1° , reducing to $1/3^{\circ}$ in the tropics.

HadGEM3-GC3.1-LL (GC3.1-LL) is the low-resolution version of the HadGEM3 coupled climate model used for CMIP6 simulations (Kuhlbrodt et al. 2018). The atmospheric component is the Unified Model GA7.1 configuration at N96 horizontal resolution (which equates to ~ 135 km in the extratropics) with 85 vertical levels up to a model lid at 85 km (35 levels are above 18 km). The ocean component is based on the NEMO ocean model in the GO6.0 configuration at 1° resolution with 75 levels. The CICE model is used for sea ice

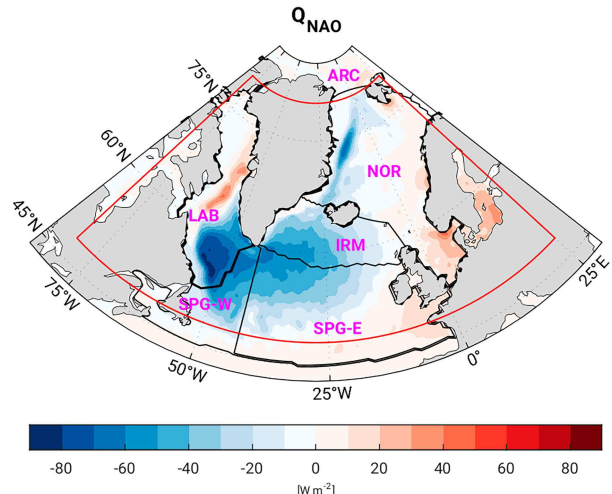


FIG. 1. Winter (December–March) NAO-related heat flux anomaly (positive into the ocean) imposed in the models. The domain outlined by the red line indicates the region where the forcing is applied with full strength and the outside of the red line (to the outer line) is a transition zone. The black lines indicate the domains where water-mass transformation is computed with the domain names indicated by pink text where SPG-W and SPG-E are the western and eastern subpolar gyre, respectively; LAB is the Labrador Sea; IRM is the Irminger Sea; NOR is the Nordic seas; ARC is the Arctic Ocean.

(GSI8.1) and land surface processes are represented using the JULES model (GL7.0). More details about the development of the GC3.1-LL are given in Kuhlbrodt et al. (2018). It is worth noting that the configuration of NEMO used in GC3.1-LL is very close to that used in EC-Earth3P other than a few parameters related to horizontal mixing and turbulent kinetic energy parameterizations.

b. Experimental design

We impose surface heat flux anomalies equivalent to 2 standard deviations of the observed winter [December–March (DJFM)] NAO in the ocean component of each model over the SPNA. This amplitude of the NAO heat flux forcing is larger than the decadally averaged amplitude in observations, which is only about 1.2 standard deviation during the decades from the early 1960s to the mid-1990s when there were large multidecadal changes. This amplitude choice was made to obtain clear response signals, particularly in the atmosphere where the signal-to-noise ratio is unrealistically low, possibly due to the low resolution of the models (Scaife et al. 2019). The surface heat flux anomalies are derived from ERA5 (Hersbach et al. 2020). Specifically, the anomalous forcing is obtained by regressing the anomalous DJFM ERA5 total (turbulent plus radiation) surface heat fluxes onto the station-based DJFM NAO index (Hurrell 1995), without applying any temporal smoothing, using the data from 1979 through 2018 (Fig. 1).

This anomalous heat flux forcing (Q_{NAO}) is added to the net heat flux passing from the coupler to the ocean component (Q_c) at each time step as follows:

$$Q_o = Q_c + Q_{\text{NAO}}^{\text{eff}}, \quad (1)$$

where Q_o is the net heat flux into the ocean component and $Q_{\text{NAO}}^{\text{eff}}$ is the effective NAO heat flux forcing received by the ocean:

$$Q_{\text{NAO}}^{\text{eff}} = Q_{\text{NAO}} \times (1 - a_i) \times W_t(t) \times W_A(x, y), \quad (2)$$

where a_i is the sea ice fraction simulated by the model; $W_t(t)$ is the temporal weight of the forcing, set to 1 for mid-December through mid-March, with a linear transition from mid-November and to mid-April (zero otherwise); $W_A(x, y)$ is the spatial weight of the forcing, set to 1 within the SPNA region bounded by 48°–80°N, 80°W–25°E (solid red line in Fig. 1), with a 5° linear transition to zero on each side of the forcing domain (the border of Fig. 1). We stress that only the ocean component is perturbed by the forcing while other components exchange fluxes without any constraint. That being said, heat is not conserved within the coupled system when the forcing is applied.

Two parallel coupled ensembles have been conducted, corresponding to positive and negative NAO forcing. The ensemble size is either 20 (CESM2 and GC3.1-LL) or 25 (EC-Earth3P) (Table 1). The forcing is applied for the first 10 winters and the simulations continue for another 10 (GC3.1-LL) or 20 (CESM2 and EC-Earth3P) years. All simulations are initialized on 1 January and the forcing is switched on as soon as the run starts. The forcing of the first winter is therefore only imposed over the months of January–April and because of this reason, we use January–March (JFM) winter averages in the following analyses. Initial conditions are taken from the pre-industrial control simulations of each model and external forcing is fixed at 1850 conditions during the experiments. We select a “neutral” set of initial conditions by verifying that the 20 years following the selected initial conditions in the pre-industrial control simulations do not exhibit significant decadal anomalies or drift in key variables such as AMOC and SPNA UOT in the ensemble average.

c. Computing the surface water mass transformation and surface water mass formation

The volume of water being transformed at given density classes to another classes by surface density fluxes (i.e., surface WMT) is computed using a widely used method (e.g., Speer and Tziperman 1992; Grist et al. 2014; Petit et al. 2021) based on a pioneering work by Walin (1982). Specifically, we adopt the details used in Yeager et al. (2021), including the

TABLE 1. Summary of the horizontal and vertical resolutions of the ocean models, simulation length, and ensemble size for each \pm NAO experiment. The vertical resolution shown in the first row is the number of layers. The simulation length includes the first 10 years with the forcing.

	CESM2	GC3.1-LL	EC-Earth3P
Horizontal/vertical resolution	1°/60	1°/75	1°/75
Simulation length (yr)	30	20	30
Ensemble size	20	20	25

equation of state (McDougall et al. 2003), the number and range of density layers, and regions where surface density fluxes (SDF) along the outcropping density layers are integrated to compute WMT.

SDF (in units of $\text{kg m}^{-2} \text{s}^{-1}$) is calculated from the monthly net surface heat (Q_o) and freshwater (F_o) fluxes (positive into the ocean for both fluxes) from the models as follows:

$$\text{SDF} = -\frac{\alpha}{C_p} Q_o - \beta \frac{S}{1-S} F_o, \quad (3)$$

where α is the thermal expansion coefficient, C_p is the specific heat capacity of seawater, β is the haline contraction coefficient, and S is the sea surface salinity; α and β are computed using the nonlinear equation of state from McDougall et al. (2003) as mentioned above.

To obtain WMT (in $\text{m}^3 \text{s}^{-1} \equiv 10^{-6} \text{ Sv}$; 1 Sv $\equiv 10^6 \text{ m}^3 \text{s}^{-1}$) as a function of density, the SDF is integrated along surface density outcropping areas (A_ρ) north of 45°N in the Atlantic sector including the Arctic and subarctic oceans and within each domain delineated in Fig. 1:

$$\text{WMT}(\rho) = \frac{1}{\Delta\rho} \iint \text{SDF} dA_\rho, \quad (4)$$

where $\rho = \sigma_2$ (i.e., density referenced to 2000 m after subtracting 1000 kg m^{-3}) in our application. $\Delta\rho$ is 0.2 kg m^{-3} for $28 \leq \sigma_2 \leq 35 \text{ kg m}^{-3}$, 0.1 kg m^{-3} for $35 < \sigma_2 \leq 36 \text{ kg m}^{-3}$, and 0.05 kg m^{-3} for $36 < \sigma_2 \leq 38 \text{ kg m}^{-3}$ (86 layers in total). Surface water mass formation (WMF in Sv) is computed as the convergence of WMT:

$$\text{WMF}(\rho) = -\frac{d\text{WMT}}{d\rho} \times d\rho. \quad (5)$$

Thus, Eq. (5) quantifies the volume of water masses that is formed or destroyed by WMT at given density classes.

Because Q_o can be decomposed into the Q_c and $Q_{\text{NAO}}^{\text{eff}}$ terms [Eq. (1)], Eq. (3) can be decomposed into

$$\text{SDF} = -\frac{\alpha}{C_p} (Q_c + Q_{\text{NAO}}^{\text{eff}}) - \beta \frac{S}{1-S} F_o. \quad (6)$$

We note that all SDF terms can change due to the ocean surface response to imposed NAO forcing, including its effect on α and β , which are function of density. Consequently, the heat flux component of WMT and WMF can also be decomposed into terms related to Q_c , $Q_{\text{NAO}}^{\text{eff}}$, and F_o .

The ocean components in all three coupled models use depth coordinates, so the overturning streamfunction in density (σ_2) coordinates [hereafter AMOC(σ)] is computed off-line in order to be related to WMT. In the following sections, we show annually or seasonally averaged ensemble-mean differences between +NAO and -NAO experiments, which can be interpreted as the linear response to the imposed forcing. The statistical significance of the ensemble-mean difference is assessed at the 95% confidence level using a two-sided Student's t test with degrees of freedom determined using the Welch–Satterthwaite equation (Welch 1947).

3. Results

a. Comparison of background states

The present study compares ocean responses to the observed NAO-related heat flux forcing in three climate models focusing on WMT and AMOC, and thus, here we compare essential features of the background state of these variables. We define the background state as a first-year average across both +NAO and -NAO experiments, equivalent to 50- and 40-yr averages for EC-Earth3P and for CESM2 and GC3.1-LL, respectively, because a long preindustrial control simulation is not available for EC-Earth3P. Although the forcing is active for the first year, responses are generally weak and largely cancel out by averaging across both +NAO and -NAO experiments. As will be shown later, the strength of the WMT response depends on the background state of the surface density and surface heat fluxes. We will show these background states when the WMT response is discussed.

Figures 2a–c show the background state of JFM WMT for the entire Atlantic sector north of 45°N (black line) and sub-domains outlined in Fig. 1 (colored lines). All models show enhanced total WMT at densities (σ_2) roughly between 35.7 and 37 kg m⁻³, which is most pronounced in CESM2. In particular, the peak WMT between 36.7 and 36.9 kg m⁻³ is about twice as large as that of GC3.1-LL and EC-Earth3P. Much of this elevated WMT in CESM2 takes place in the LS in the higher density classes (36.8–36.9 kg m⁻³) with a contribution from the Nordic seas, while WMT in the eastern SPNA (IRM plus SPG-E) contributes much of the total WMT at lower density classes (36–36.7 kg m⁻³). Although WMT in the western SPNA (LAB plus SPG-W) is somewhat elevated in GC3.1-LL and EC-Earth3P in the high-density range as in CESM2, its strength is substantially weaker (less than 10 Sv versus more than 40 Sv), especially in EC-Earth3P, likely because of substantially weaker surface heat loss and too extensive sea ice cover in the LS (see below). As a result, no distinct peak is found for the total WMT in these density classes in these models. Instead, the total WMT in high density classes (36.5–36.9 kg m⁻³) is mostly contributed by the Nordic seas in EC-Earth3P and by multiple regions (both western and eastern SPNA and Nordic seas) in GC3.1-LL. WMT in the Arctic Ocean is more active in these models in the density classes greater 37 kg m⁻³, while much of the WMT in these densest classes takes place in the Nordic seas in CESM2. The annual background WMT shows similar shapes for all models with an amplitude approximately one-third of the JFM mean. The maximum annual surface WMT of ~10 Sv in GC3.1-LL and EC-Earth3P is consistent with observational estimates by Jackson and Petit (2023), while that in CESM2 (~20 Sv) is overestimated.

Figures 2d–f show the background state of AMOC(σ). All three models show a broadly comparable background AMOC(σ) in that most densification of northward flowing waters takes place from the subtropics through the SPNA, which feeds the southward flowing dense-water roughly denser than 36.7 kg m⁻³ in CESM2 and 36.5 kg m⁻³ in GC3.1-LL and EC-Earth3P. However, the maximum overturning strength at subpolar latitudes is substantially stronger in CESM2 (~25 Sv), roughly twice that of other two models (~13 Sv), consistent with the maximum

background WMT difference. We also note that a relatively large contribution from the Nordic and Arctic seas seen in WMT in GC3.1-LL and EC-Earth3P is also evident in AMOC(σ) (i.e., the overturning cell north of 60°N at densities greater than 36.5 kg m⁻³). In comparison to the direct measurements of the AMOC at 26.5°N (RAPID array; Moat et al. 2023), CESM2 shows relatively good agreement with the maximum overturning of ~18 Sv, compared to ~17 Sv in the observations, although the upper (North Atlantic Deep Water) cell is too shallow (Fig. S1 in the online supplemental material). In EC-Earth3P, the upper cell is even shallower, and the maximum overturning strength is too weak (~14 Sv) while GC3.1-LL lies in the middle.

b. Surface density fluxes

Figure 3 shows the differences of total SDF and SDF associated with the imposed heat flux forcing [i.e., the second term on the rhs of Eq. (6)]. The total SDF differences (Figs. 3a–c) show a buoyancy loss over almost entire SPNA (when the +NAO forcing is applied), which is largely contributed by the imposed forcing (Figs. 3d–f). The contributions coming from the other two terms on the rhs of Eq. (6), related to Q_C and F_o , whose differences are attributable to feedbacks in the coupled system in response to the forcing are minor (Fig. S2). In particular, the SDF differences due to F_o are almost negligible except along the ice edge (Figs. S2d–f). The negative differences due to Q_C arise because of a cooling driven by the imposed (positive) NAO forcing and acts to damp moderately the total SDF differences in the central SPNA (Figs. S2a–c).

Although the same heat flux forcing is originally used (Q_{NAO}), the ocean component of each model receives slightly different effective heat flux forcing due to different sea ice conditions [cf. Q_{NAO}^{eff} in Eq. (2)], particularly in the LS. The most and least extensive background sea ice cover in the LS (black lines in Figs. 3d–f) allows for the weakest and strongest heat flux forcing in EC-Earth3P and CESM2, respectively, while GC3.1-LL lies in the middle. In addition, the LS sea ice cover increases more in GC3.1-LL and EC-Earth3P for the +NAO forcing (while shrinking more for the -NAO forcing), as will be shown later, contributing to a weaker heat flux forcing in these models compared to CESM2. We note that the background sea ice extent is closest to that of satellite-derived estimates (blue lines) in CESM2, particularly in the LS. The SDF differences associated with Q_{NAO}^{eff} are further affected by background α , which is lowest in EC-Earth3 in the western SPNA, followed by GC3.1-LL and CESM2 (Figs. S3a–c). In addition, α decreases most in GC3.1-LL, followed by EC-Earth3P and CESM2 (Figs. S3d–f), as SST cools in the same order as α in response to the +NAO forcing. Because of these effects of sea ice extent and α , the total SDF differences in the western SPNA are about 30% larger in CESM2 than in GC3.1-LL, which is in turn about 40% larger than in EC-Earth3P. The differences in the eastern SPNA are relatively small (about 10% larger in CESM2 than GC3.1-LL, which is about 5% larger than in EC-Earth3P).

c. WMT/WMF response

Figure 4 shows JFM WMT (Figs. 4a–c) and WMF (Figs. 4d–f) differences, averaged over the first decade when the forcing is

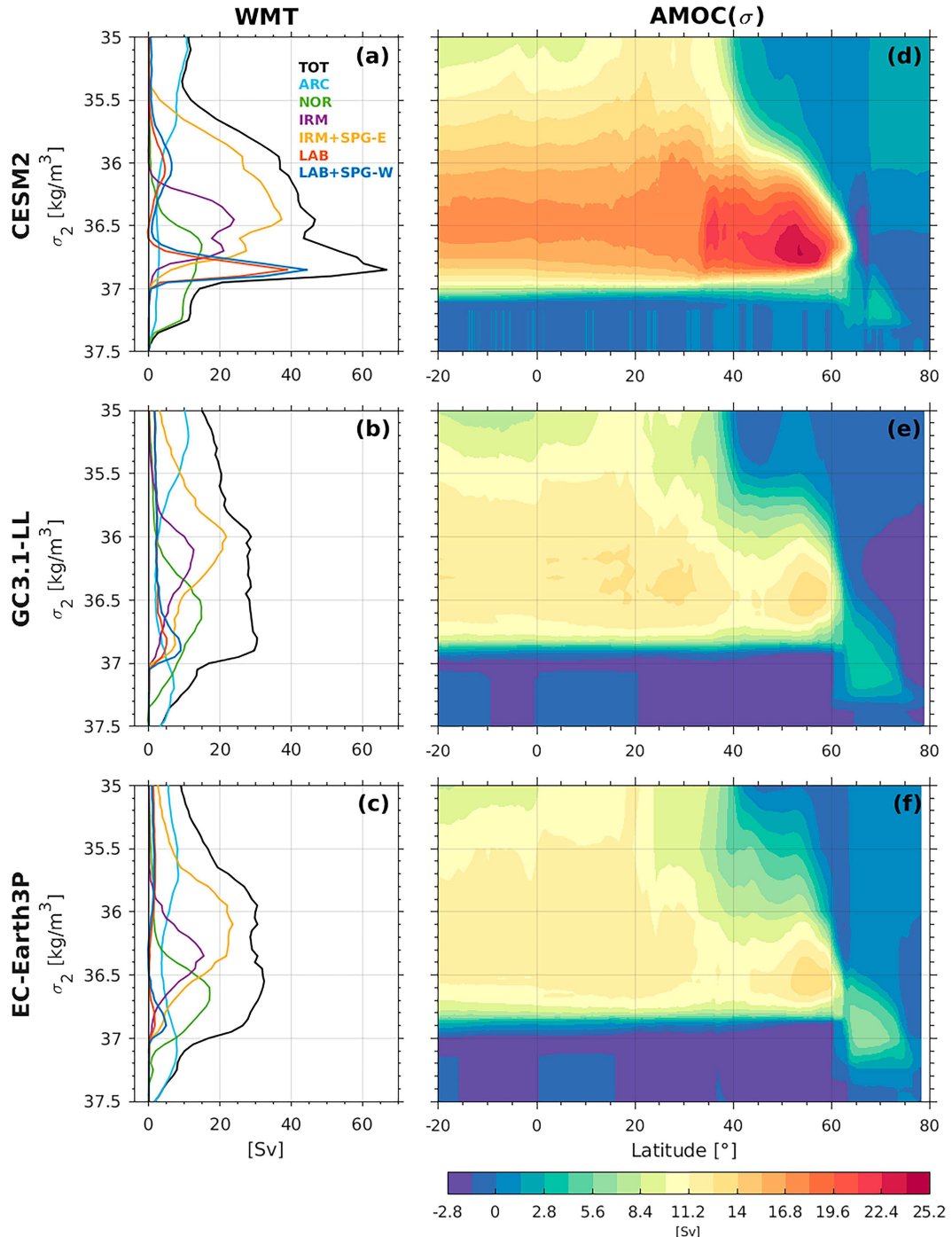


FIG. 2. Background state of (a)–(c) JFM water mass transformation (WMT) and (d)–(f) annual overturning streamfunction in density (σ_2) coordinates from (top) CESM2, (middle) GC3.1-LL, and (bottom) EC-Earth3P. In (a)–(c), each line represents WMT in the entire North Atlantic domain north of 45°N (black), ARC (light blue), NOR (green), IRM (purple), IRM plus SPG-E (yellow), LAB (red), and LAB plus SPG-W (blue) domains shown in Fig. 1.

applied, as a function of σ_2 . Integrated over the entire domain north of 45°N , all models show a strong increase in WMT in the high-density class between 36.8 and 37 kg m^{-3} (black lines in Figs. 4a–c) and weaker (generally positive) WMT change over a

broad range of lighter densities. The density range of the peak response is similar to or denser than that of the background WMT peak (Figs. 2a–c). As WMT is the convergence of WMT [Eq. (5)], the high-density WMT anomaly peak corresponds to a

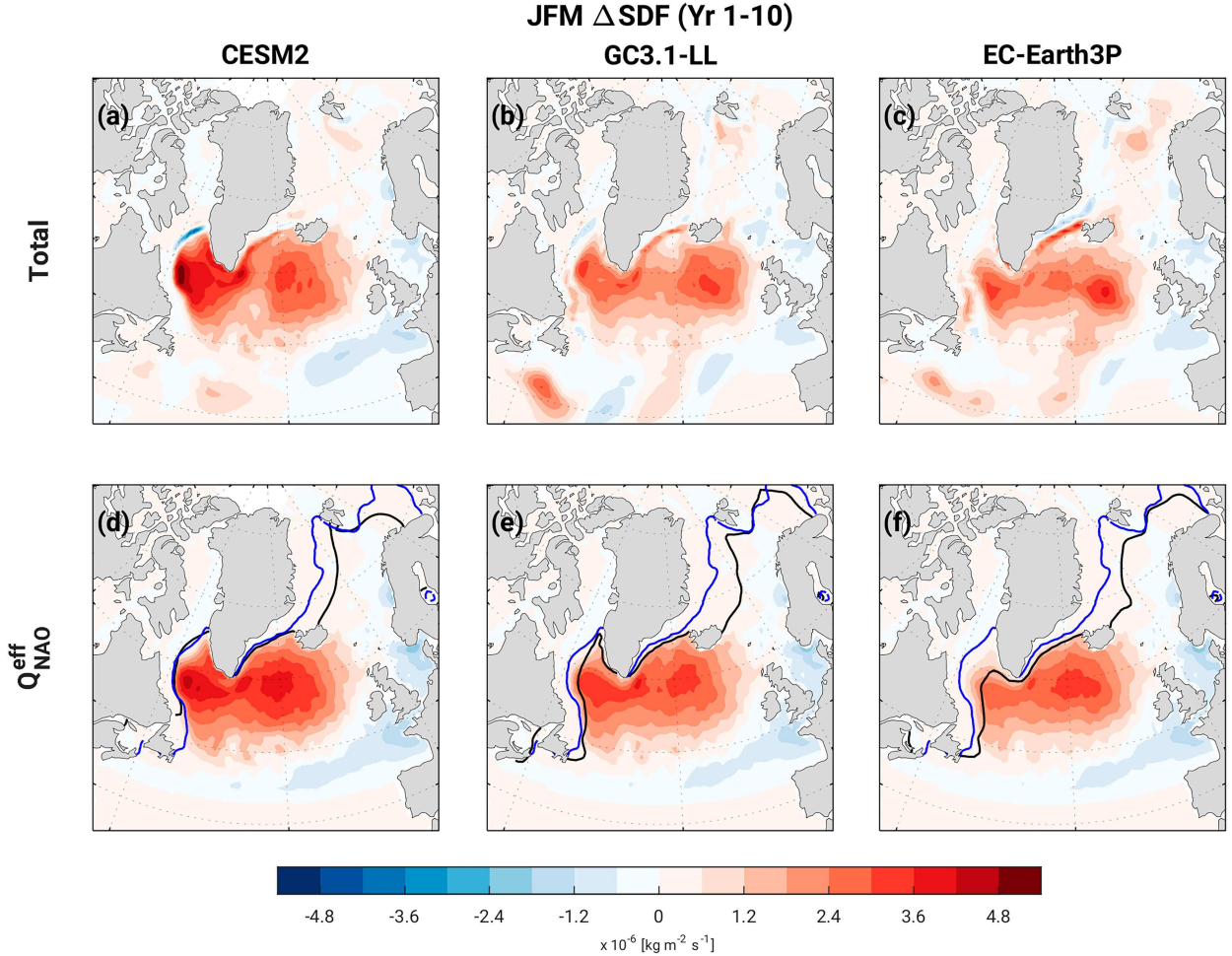


FIG. 3. Differences (+NAO minus $-\text{NAO}$ experiment) of January–March (JFM) (a)–(c) total surface density flux (SDF) and (d)–(f) SDF associated with the effective NAO forcing [$Q_{\text{NAO}}^{\text{eff}}$, the second term on the rhs of Eq. (6)], averaged over the first decade (years 1–10), from (left) CESM2, (center) GC3.1-LL, and (right) EC-Earth3P. The black and blue lines in (e) and (f) represent the background JFM sea ice extent (15% ice concentration) simulated in each model and from satellite-derived estimates (1979–2014 average; Comiso 2000), respectively.

dipole WMF response (Figs. 4d–f). That is, the imposed +NAO forcing produces a densification of high-density water masses that make up the AMOC lower limb. While all models exhibit qualitatively similar WMT/WMF responses, the strength of the peak response is more than twice as large in CESM2 compared to the other models. We will discuss this different response strength later in this subsection.

Despite the fact that the primary background high-density WMT takes place in regions other than the western SPNA in GC3.1-LL and EC-Earth3P (Fig. 2), the WMT/WMF peak response is mostly contributed by the western SPNA in all models (red lines in Fig. 4). In GC3.1-LL and EC-Earth3P, there is a relatively large contribution from the eastern SPNA (blue lines), which is the largest contribution for lighter density classes (~ 36.0 – 36.7 kg m^{-3}) in all models. The importance of the western SPNA is especially clear in CESM2 where the peak response of WMT and the associated dipole WMF response are dominated by the LS (Figs. S4a,d). In contrast, the contributions from the LS, SPG-W, and SPG-E are all comparable

in GC3.1-LL and EC-Earth3P (Figs. S4b–c and e–f). Although the maximum peak WMT difference in the western SPNA is roughly 3 times larger in CESM2 than in the other two models, the total WMT difference integrated over density classes of the respective broad peaks ($>36.0 \text{ kg m}^{-3}$) is about twice as large in CESM2 compared to GC3.1-LL, which is in turn about 50% larger than in EC-Earth3P. This intermodel difference is much larger than the intermodel SDF difference discussed above can explain. There is also an anomalous WMT/WMF in the Irminger Sea in all models, but it mostly occurs in a lighter σ_2 range ($<36.8 \text{ kg m}^{-3}$). The WMT/WMF response in the Nordic seas and the Arctic Ocean is negligible (not shown). The contribution from freshwater flux to the WMT/WMF response is also relatively small, especially in CESM2 (Fig. S4). In all models, but especially in GC3.1-LL and EC-Earth3P, the WMT response due to freshwater flux tends to damp the enhanced WMT in high-density classes (36.7 – 36.9 kg m^{-3}).

Although the WMT (and thus WMF) response is ultimately a consequence of the imposed forcing, we find a surprisingly

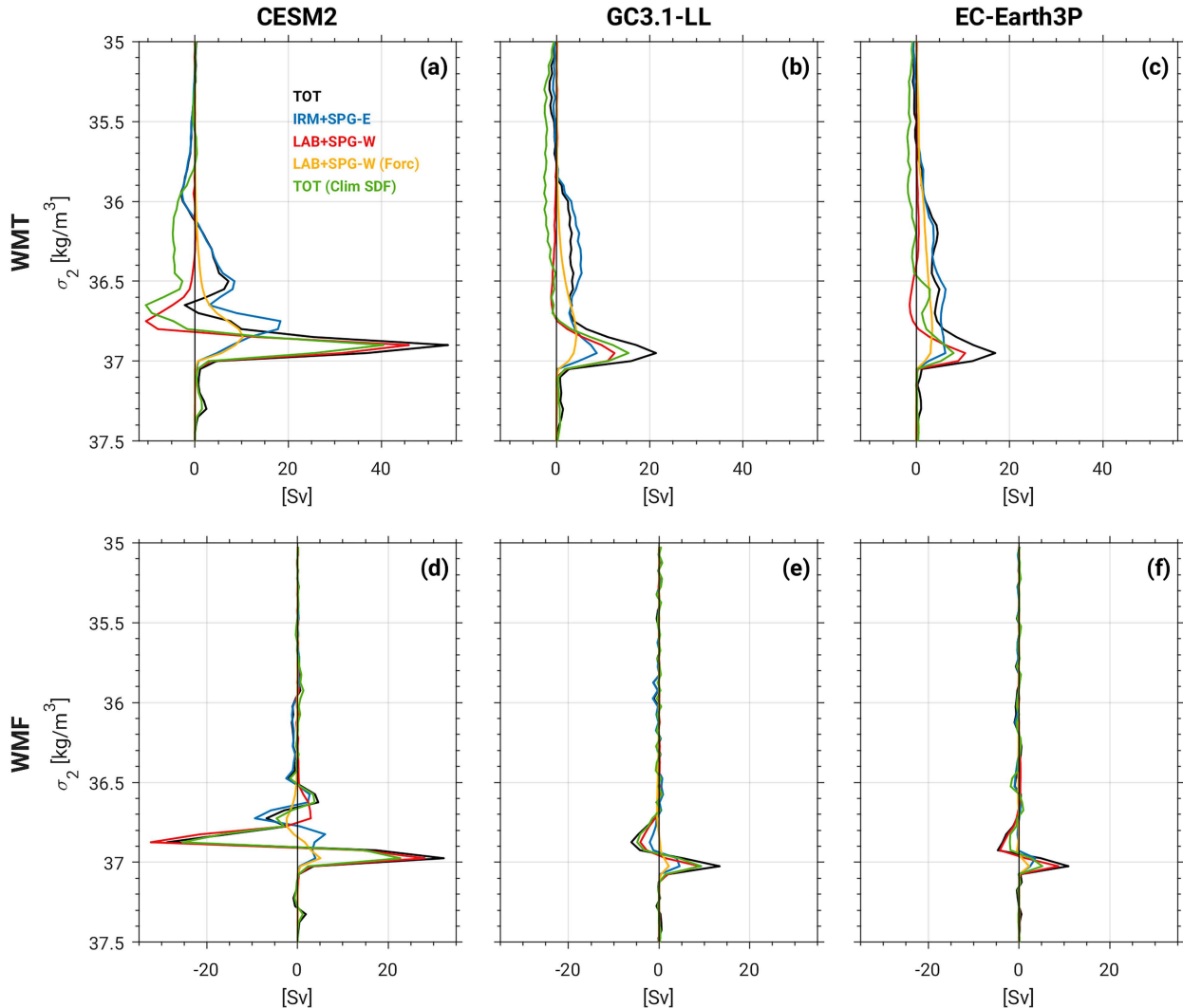


FIG. 4. Differences of (a)–(c) JFM water mass transformation (WMT) and (d)–(f) water mass formation (WMF), averaged over the first decade, from (left) CESM2, (center) GC3.1-LL, and (right) EC-Earth3P. The colored lines represent the differences in the entire North Atlantic domain north of 45°N (black), eastern SPNA (IRM plus SPG-E; blue), western SPNA (LAB plus SPG-W; red), and due to the imposed forcing in the western SPNA (yellow). The green lines are same as black lines but computed with the background SDF and time-varying isopycnal outcropping area.

small WMT/WMF response associated with $Q_{\text{NAO}}^{\text{eff}}$ (yellow lines in Fig. 4), which appears to account for only a small fraction (<20%) of the peak WMT/WMF response and occurs over lighter density classes than those of the enhanced total WMT/WMF response. This result may appear at odds with the dominance of $Q_{\text{NAO}}^{\text{eff}}$ in the SDF differences (Fig. 3), but the WMT response also depends on changes in isopycnal outcropping area [A_{ρ} ; Eq. (4)]. We note that changes in A_{ρ} are already taken into account in the WMT/WMF response associated with $Q_{\text{NAO}}^{\text{eff}}$. Therefore, much of the WMT/WMF response should result from interaction between Q_C and A_{ρ} , although the SDF differences due to Q_C itself are small (Fig. S2).

Figure 5 shows the JFM A_{ρ} differences for the first decade in the western (solid red lines) and eastern (solid blue lines)

SPNA along with their background states (dashed lines). All models reveal the peak response of A_{ρ} in density classes where the respective peak WMT response occurs (Fig. 4). A_{ρ} increase occurs at densities slightly greater than the highest density of the background outcropping area, at the expense of a decrease at lighter densities, indicating an expansion of dense A_{ρ} in the SPNA when the positive NAO heat flux forcing is applied. Similar to the WMT response, the maximum (positive) A_{ρ} change in the western SPNA is largest in CESM2 (roughly twice as large compared to the other two models), but the intermodel difference is smaller than that of WMT. Therefore, other factors seem to be needed to explain the intermodel difference of the magnitude of the WMT response. We note that the A_{ρ} changes take place over a wider density range in GC3.1-LL and EC-Earth3P, while they are

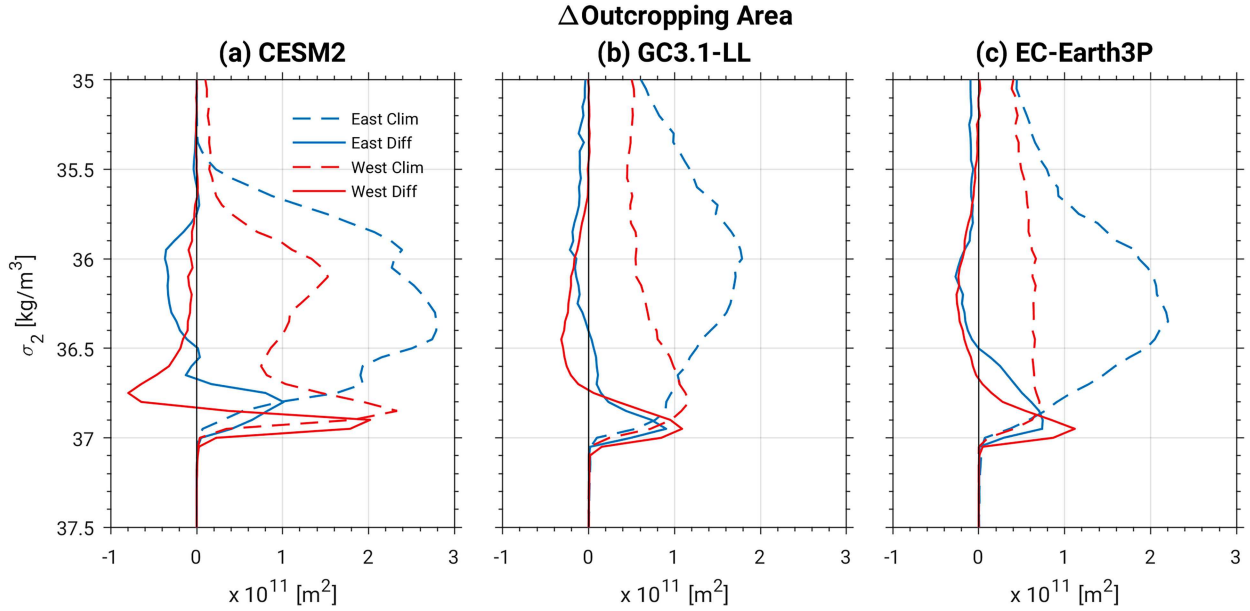


FIG. 5. Differences of JFM isopycnal outcropping area averaged over the first decade (solid) in the western (red; LAB plus SPG-W) and eastern (blue; IRM plus SPG-E) SPNA. Also, shown are the respective background state of the isopycnal outcropping area (dashed).

concentrated in the highest density classes in CESM2, which is also generally consistent with the WMT changes (Figs. 4a–c).

The expansion of A_p toward higher densities implies that these density layers are exposed to surface heat loss by the background surface heat flux, which is intense in the western SPNA. Figure 6 shows the JFM surface density (σ_2), averaged over the first decade, from the +NAO experiment (red contours) in the western to central SPNA along with the background JFM surface heat fluxes (shading) and first-decade average JFM sea ice edge (15%) from the +NAO experiment (light blue contours). The expansion of A_p of $36.8\text{--}37.0\text{ kg m}^{-3}$ (note the difference between the black and red contours of 36.8 kg m^{-3}) is most obvious, compared to other layers, in all models, especially in CESM2, consistent with Fig. 5. This expanded A_p coincides with strong background surface heat fluxes, reaching up to 400 W m^{-2} in the LS around 60°N in CESM2 but $250\text{--}300\text{ W m}^{-2}$ in GC3.1-LL and around 200 W m^{-2} in EC-Earth3P. In EC-Earth3P, moreover, the LS is more covered by sea ice, thus the background surface heat flux feedback is less efficient there. Therefore, these results suggest that changes in A_p and associated changes in surface WMT from the background surface heat fluxes are the key processes that determine the WMT response to the imposed forcing. That is, the WMT response is especially larger in CESM2 because the expanded A_p is exposed to a greater background surface heat loss.

To verify the above hypothesis, we repeat the computation of WMT/WMF with background SDF. That is, A_p only changes in time in this computation. The resultant total WMT/WMF differences averaged over the first decade are shown as green lines in Fig. 4. The WMT/WMF with background SDF indeed explains a large portion of the total

WMT/WMF: more than 70% in CESM2 and GC3.1-LL, and about 50% in EC-Earth3P, confirming the key role of changes in A_p and associated changes in surface WMT from the background surface heat fluxes for the total WMT/WMF differences. A quantitatively similar conclusion also holds when the western SPNA is separately considered. We note that the weaker response of WMT/WMF with background SDF in EC-Earth3P, compared to GC3.1-LL, reflects the weaker background surface heat fluxes in this model, as changes in outcropping area are comparable between the two models.

d. AMOC response

Based on the WMT analysis, we would expect the AMOC(σ) response roughly to be twice as large in CESM2 as in GC3.1-LL and EC-Earth3P. Figure 7 shows decadal AMOC(σ) responses superimposed on the background states. In all models, an increase in lower (denser) limb of AMOC(σ) is observed during the first decade at subpolar latitudes (north of 45°N), at densities greater than the density where the background maximum overturning takes place and similar to the density range where anomalous WMT occurs (Figs. 7a–c). The amplitude difference of the maximum lower limb response, which is twice or more as large in CESM2 as in the other two models ($\sim 10\text{ Sv}$ in CESM2 vs $\sim 4\text{ Sv}$ in GC3.1-LL and EC-Earth3P; note the different color scales in Fig. 7), indeed matches roughly that of the peak WMT response. In the second decade (years 11–20; Figs. 7d–f), there is an indication of a southward propagation of the overturning anomalies in all three models within the lower limb, seen most prominently in CESM2. In GC3.1-LL and EC-Earth3P, there appears to be a greater communication of the signal to lighter waters during the propagation to the south. Interestingly, the response of the upper (lighter) limb at

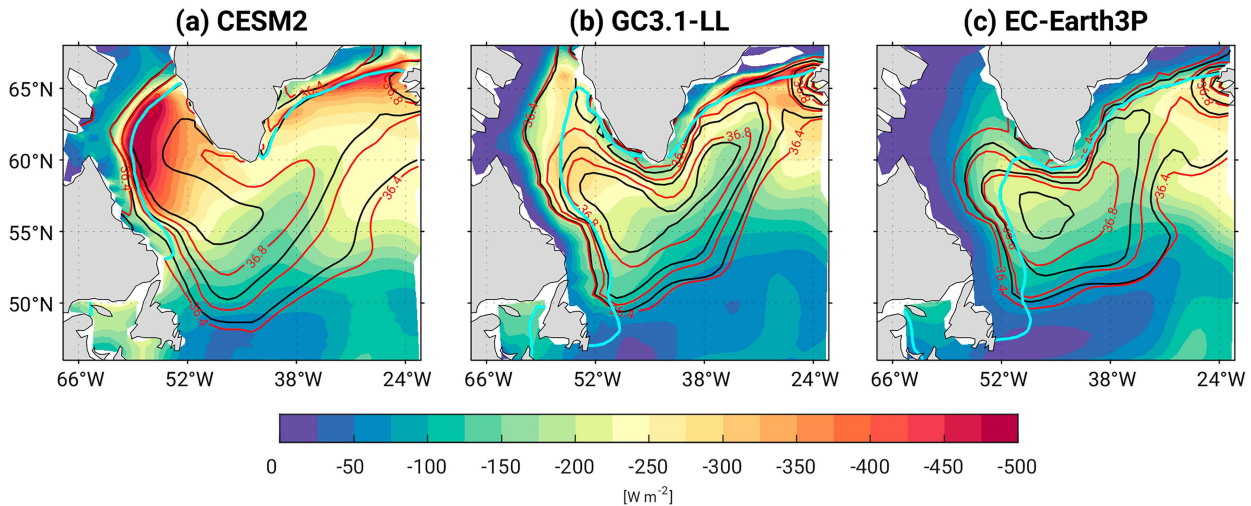


FIG. 6. JFM surface density (σ_2) from the ensemble mean of +NAO experiments (red contours) and its background state (black contours), superimposed on the background JFM surface heat fluxes (shading; negative for heat loss from the ocean), from (a) CESM2, (b) GC3.1-LL, and (c) EC-Earth3P. Also shown is the JFM sea ice extent (15%) from the ensemble mean of +NAO experiments (cyan). For σ_2 , only contours greater than 36.4 kg m^{-3} are shown at intervals of 0.2 kg m^{-3} . Note that the color scale for the surface heat fluxes is reversed.

subpolar latitudes, the northward flow at densities lighter than the density of the background maximum overturning, emerges as the lower limb anomaly propagates to the south in all models (cf. Figs. 7a–c and d–f) and persists even after the lower limb anomalies dissipate and move to the subtropics (Figs. 7g,h). Notably, this upper limb response appears as a secondary maximum between densities 36 and 36.5 kg m^{-3} in CESM2 during the second and third decades (Figs. 7d,g) and in EC-Earth3P during the third decade (Fig. 7h).

The overturning streamfunction in depth coordinates [AMOC(z)] also shows a consistent pattern of decadal differences across the models (Fig. S5) with an anomalous overturning, centered at around 1000 m (slightly deeper in CESM2), propagating from subpolar latitudes ($40\text{--}60^\circ\text{N}$) during the first decade to subtropical latitudes in the later decades. Consistent with the AMOC(σ) response, the amplitude of the AMOC(z) response is also substantially stronger in CESM2 than in the other two models (~ 3.2 vs $\sim 1.8 \text{ Sv}$ in terms of the maximum overturning anomalies). We note that the delayed response of the upper limb at subpolar latitudes seen in AMOC(σ) is not seen in AMOC(z) in all models, consistent with the idea that the delayed signal is a gyre circulation response that becomes visible when overturning is viewed in density space (Yeager 2020; Yeager et al. 2021).

Yeager (2020) put forward a mechanism that clarifies the connection between the upper and lower limbs of AMOC(σ) that involves deep, dense-water flow interacting with bottom topography. The Mid-Atlantic Ridge (MAR) acts as a dam for southeastward flowing dense waters formed in the SPNA and causes these dense waters to accumulate along its western flank near the southern boundary of the SPNA. The accumulation of anomalously dense waters in this region generates a corresponding SSH anomaly through the steric effect. The zonal gradient of the SSH anomaly drives an anomalous

meridional geostrophic flow that projects onto the upper limb of AMOC(σ) and brings warm subtropical waters into the SPNA. Away from the influence of surface fluxes and stalled by the MAR, this dense water anomaly persists in time and, hence, provides high predictability of the upper limb of AMOC(σ) and UOT in the SPNA. This mechanism has also been identified in a multicentennial, high-resolution (eddy-rich) coupled simulation using CESM (Yeager et al. 2021).

In line with this proposed mechanism, we find a similar propagation and accumulation of dense-water thickness anomalies around the MAR in all models, with patterns that are consistent with concurrent SSH anomalies (Fig. S6). In Figs. 8a–c, we show dense-water thickness ($\sigma_2 > 36.8 \text{ kg m}^{-3}$; shading) differences together with SSH differences (contours) along the models' zonal grid line closest to 45°N (roughly the boundary between the subtropical and subpolar gyres). We refer to this dense-water thickness as LS Water (LSW) thickness since much of it is generated in the LS in all models. The LSW thickness anomalies gradually increase but remain largely confined west of 30°W (i.e., west of the MAR) in all models, peaking at years between 10 and 20 with the largest thickness anomaly in CESM2 (up to 500 m). The patterns of the overlying SSH anomalies essentially mirror those of the LSW thickness anomalies. Figures 8d–f show anomalous zonal SSH gradient (shading) and meridional velocity averaged over upper 700 m (contours). The anomalous SSH gradient is largest around 30°W in all models, which is largest in CESM2 and weakest in GC3.1-LL. Through geostrophy, the positive zonal SSH gradient induces an anomalous northward flow that almost perfectly overlies the zonal SSH gradient anomaly in all models. 30°W is where the major branch of the models' North Atlantic Current (NAC) is located (Fig. S7). Thus, the anomalous northward flow can be interpreted as a strengthened NAC.

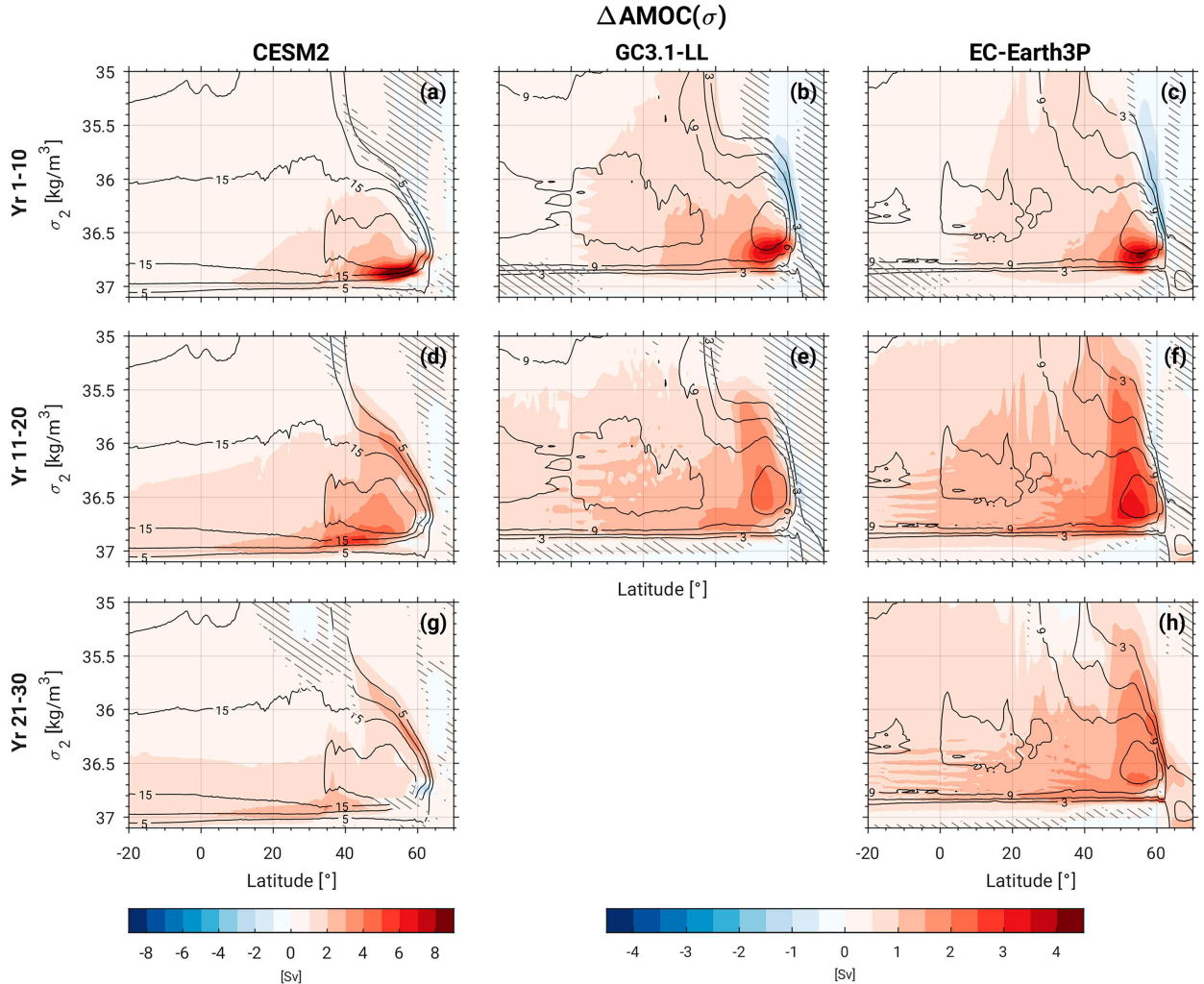


FIG. 7. Difference of annual overturning streamfunction in density (σ_2) coordinates [AMOC(σ)] averaged over (a)–(c) years 1–10, (d)–(f) years 11–20, and (g),(h) years 21–30 from (left) CESM2, (center) GC3.1-LL, and (right) EC-Earth3P. Note that the color scale for GC3.1-LL and EC-Earth3P is half of that for CESM2. The black contours are the climatological AMOC(σ) in each model with contour intervals of 5 (3) Sv for CESM2 (GC3.1-LL and EC-Earth3P). The hatched regions indicate that the differences are *not* statistically significant at a 95% confidence level.

In CESM2, the NAC anomaly peaks between years 10 and 15 and weakens by years 20–25. However, together with the secondary northward flow anomaly east of the MAR near 20°W, the total northward flow persists through the end of the simulations. In EC-Earth3P, the NAC anomaly develops around year 10, maximizes around year 18, and persists through the end of the simulations. There is also an anomalous meridional flow of opposite sign along the western boundary in all models, which cancels, to a large extent, the NAC anomaly. This cancellation is likely the reason why there is no delayed upper AMOC(z) response (Fig. S5). However, because these two anomalous meridional flows of opposite sign carry different density classes (i.e., relatively dense subpolar water along the western boundary and relatively light subtropical waters by the NAC; Fig. S8), AMOC(σ) reveals an anomalous overturning in its upper limb in the later years

(Fig. 7). In GC3.1-LL, the NAC anomaly develops after year 10, similar to other two models. However, another northward flow anomaly develops around 42°W earlier in the simulations. A similar anomalous flow also presents at a similar location in other models, but the cancellation by the opposite flow near the western boundary is weak in GC3.1-LL. This appears to be the reason for the earlier spinup of the upper AMOC(σ) limb in GC3.1-LL than in the other two models, as will be shown later.

e. Wider impacts

The anomalously strong NAC at the gyre boundary implies that more warm and salty waters are advected into the SPNA from the subtropics. Figure 9 shows that the decadal upper-ocean (500 m) temperature anomalies evolve in line with the NAC anomalies. While the forcing directly generates a

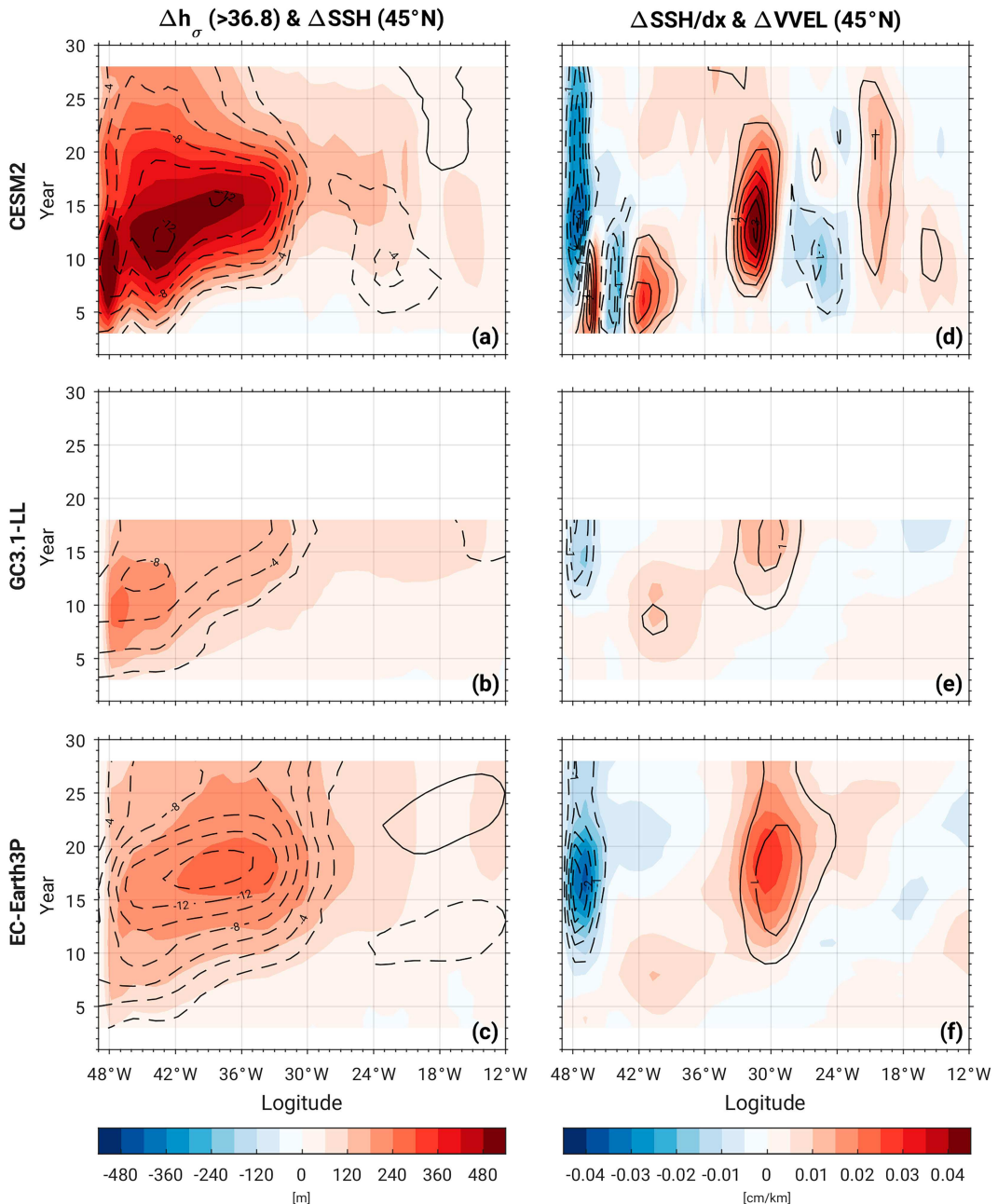


FIG. 8. Difference of (a)–(c) annual dense-water ($\sigma_2 > 36.8 \text{ kg m}^{-3}$) thickness (shading) and SSH (contours), and (d)–(f) zonal SSH gradient (shading) and meridional velocity averaged over the upper 700 m (contours), as a function of longitude (x axis) and time (y axis), along the models' zonal grid line closest to 45°N from (top) CESM2, (middle) GC3.1-LL, and (bottom) EC-Earth3P. The contour intervals are 2 cm in (a)–(c) and 0.5 cm s^{-1} in (d)–(f) with negative contours dashed and the zero contour omitted. 48°W is roughly where the continental break is located at the latitude. A 5-yr running average is applied to all time series.

cooling in the SPNA (when the +NAO forcing is imposed) for the first decade (Figs. 9a–c), this cooling is replaced by a much stronger warming in the eastern SPNA during the second decade (Figs. 9d–f). This warming develops over much of the SPNA and persists even in the third decade in CESM2 and EC-Earth3P (Figs. 9g–h). The signal-to-noise ratio of SST

exceeds 50% over much of the eastern SPNA during the second decade and even reaches 80% in EC-Earth3P at the core of the warming (Fig. S9). The strong heat flux forcing that we impose, equivalent to 2 standard deviations of the NAO, should also be a factor in this large signal-to-noise ratio. Nevertheless, this suggests that a substantial fraction of the

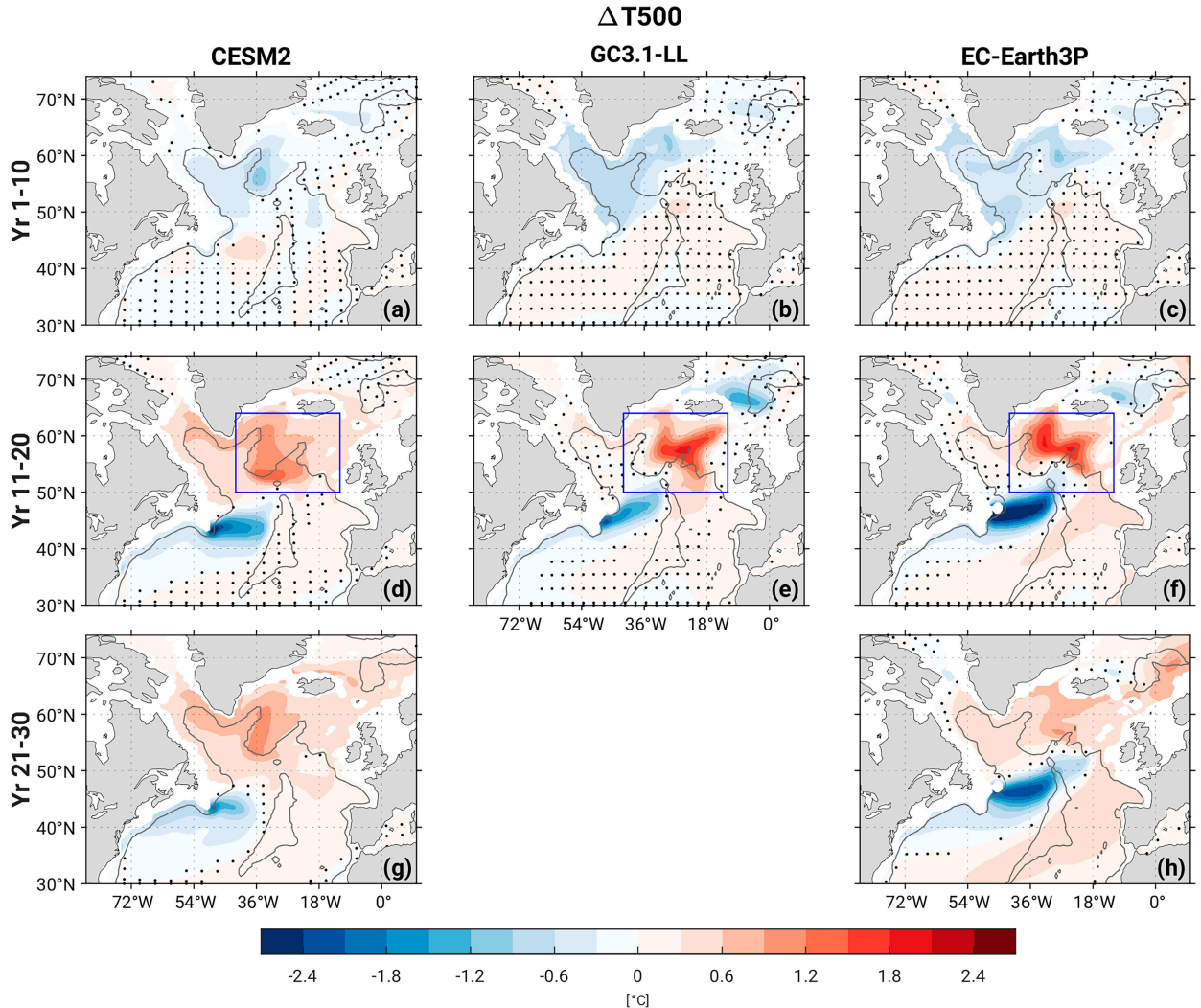


FIG. 9. Difference of annual upper 500-m temperature averaged over (a)–(c) years 1–10, (d)–(f) years 11–20, and (g),(h) years 21–30 from (left) CESM2, (center) GC3.1-LL, and (right) EC-Earth3P. The stippled regions indicate that the differences are *not* statistically significant at a 95% confidence level with every fourth stippling shown. The gray contour indicates the 3000-m isobath. The blue box indicates the region where the SPNA upper 500-m temperature time series in Fig. 4 is averaged.

decadal SST variability in the eastern SPNA in these models can be explained by the NAO-forced thermohaline processes. Concurrent with the warming in the SPNA, a cold anomaly appears off the Grand Banks west of the MAR, generating a dipole anomaly pattern in all models (Figs. 9d–h). This dipole pattern has been highlighted as a fingerprint of anomalous AMOC strength (Zhang 2008). The anomalous upper-ocean salinity pattern closely resembles that of the UOT for the last two decades (Fig. S10). In the absence of forcing that can directly impact upper-ocean salinity during the first decade, the upper-ocean salinity response in the SPNA is minor. The spatial patterns of both anomalous UOT and salinity are remarkably similar across the models, suggesting that the response of the ocean dynamics to the imposed forcing is consistent across the models regardless of different choices of model numerics and parameterizations. The decadal surface heat flux differences

for the second and third decades exhibit a heat release from the ocean in the SPNA (Fig. S10), particularly in the eastern SPNA where the anomalous UOT warms most in all models. This underpins that the SPNA temperature anomalies are driven by the heat convergence associated with the anomalous upper limb AMOC(σ), which is further supported by the paired upper-ocean salinity anomalies.

Figure 10 shows the time series of the UOT differences averaged over the eastern SPNA (boxed region in Figs. 9d–f) along with the time series of the maximum and the upper limb of AMOC(σ) differences at 45°N. The upper AMOC(σ) limb is defined at σ_2 where the anomalous northward transport is largest in each model (Fig. 7). The UOT, which initially cools under the forcing, ramps up starting from year 5, reaches a positive maximum around year 15, and stays in an anomalously warm state through the end of the simulations in

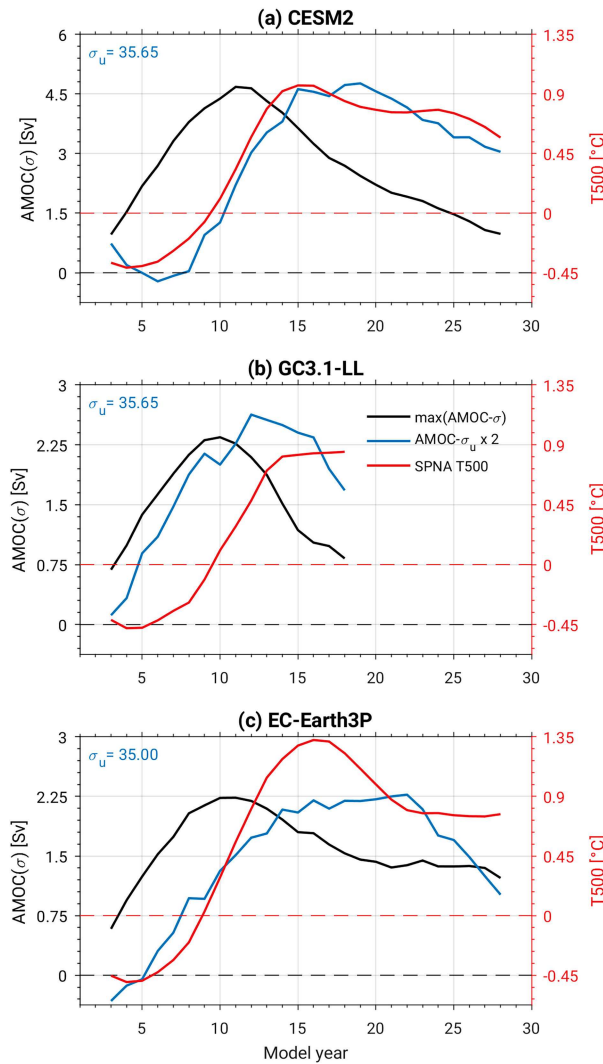


FIG. 10. Time series of annual maximum $AMOC(\sigma)$ (black) and upper limb of $AMOC(\sigma)$ (blue), defined at the density shown in the upper left corner of each panel, and the upper 500-m temperature averaged over the region in the eastern SPNA (52° – 64° N, 15° – 40° W) from (a) CESM2, (b) GC3.1-LL, and (c) EC-Earth3P. A 5-yr running average is applied for all time series.

all models. This tendency is generally consistent with the delayed spinup of the upper $AMOC(\sigma)$ limb relative to the lower $AMOC(\sigma)$ limb in all models, supporting the idea that surface northward heat transport convergence associated with the anomalous upper limb of AMOC is responsible for delayed UOT changes in the SPNA (Yeager 2020). As discussed earlier, the upper $AMOC(\sigma)$ limb increases earlier than the UOT in GC3.1-LL likely because of another anomalous meridional flow that develops early west of the NAC (Fig. 8).

Figure 9 also shows that the SPNA temperature anomalies expand to the north into the Nordic seas and to the west into the LS, particularly evident during the third decade. This suggests that sea ice in the Nordic seas and Labrador Sea can be affected by the temperature anomalies. The JFM sea ice

concentration differences (Fig. 11) confirm a delayed sea ice response to NAO forcing. With the arrival of the warm anomaly in the SPNA, all models show a sea ice concentration decrease along the sea ice edge, especially in the LS in the second decade (Figs. 11d–f). With the extension of the warm anomaly to the Nordic seas in CESM2 and EC-Earth3P (Figs. 9d,f), sea ice concentration also decreases there (Figs. 11d,f), which is further amplified in the third decade (Figs. 11g,h) as the warming further builds up in the Nordic seas (Figs. 9g,h). The sea ice concentration decrease is substantially stronger in EC-Earth3P than other two models with more than 30% (20%) decrease in the Barents Sea (the Greenland Sea), consistent with a greater warming in the Nordic seas than other models. These findings support previous studies (e.g., Mahajan et al. 2011; Yeager et al. 2015) that have demonstrated how AMOC-driven SPNA UOT anomalies can penetrate into the Nordic seas to drive decadal sea ice variability there.

4. Summary and discussion

We examine in the present study the response of the North Atlantic to winter NAO-related surface heat flux forcing derived from observational estimates using three CMIP6-class coupled models (CESM2, GC3.1-LL, and EC-Earth3P). The primary focus of the study is to explore the robustness of mechanisms that connect surface-forced WMT/WMF to AMOC strength and associated UOT changes in the SPNA. By focusing on ensemble-mean coupled model response to observation-based NAO forcing, we circumvent biases in each model's own representation of NAO-related surface heat fluxes. This allows for a systematic comparison of the responses to the observed NAO across models that have different background states.

The experiments reveal a broadly consistent picture of the ocean responses across the models that support the idea that ocean thermohaline processes play a critical role in NAO-driven changes in UOT and salinity in the SPNA. Although the models produce deep waters at different locations in the background state (western SPNA in CESM2, and eastern SPNA and Nordic seas in GC3.1-LL and EC-Earth3P), the forcing promotes the largest WMT response consistently in the western SPNA in all models. In the case of +NAO forcing, this WMT response increases the volume of the densest SPNA water masses, leading to a densification and enhancement of the lower (denser) $AMOC(\sigma)$ limb in the SPNA. The anomalous dense waters generate a zonal pressure (SSH) gradient anomaly through the steric effect around the southern boundary of the SPNA west of the MAR, as they propagate to the south, thus driving an anomalous northward flow in the upper ocean, corresponding to the upper (lighter) limb of $AMOC(\sigma)$. The anomalous northward flow, equivalent to a strengthening of the NAC, brings more warm and salty subtropical waters into the SPNA, increasing heat and salt content in the SPNA in all models with reverberations on sea ice conditions in the subarctic Atlantic Ocean. The spatial patterns of these responses are strikingly similar between the models, suggesting that the dynamical ocean responses are similar across the models despite the different choices of model numerics and physics. In contrast to the consistent spatial

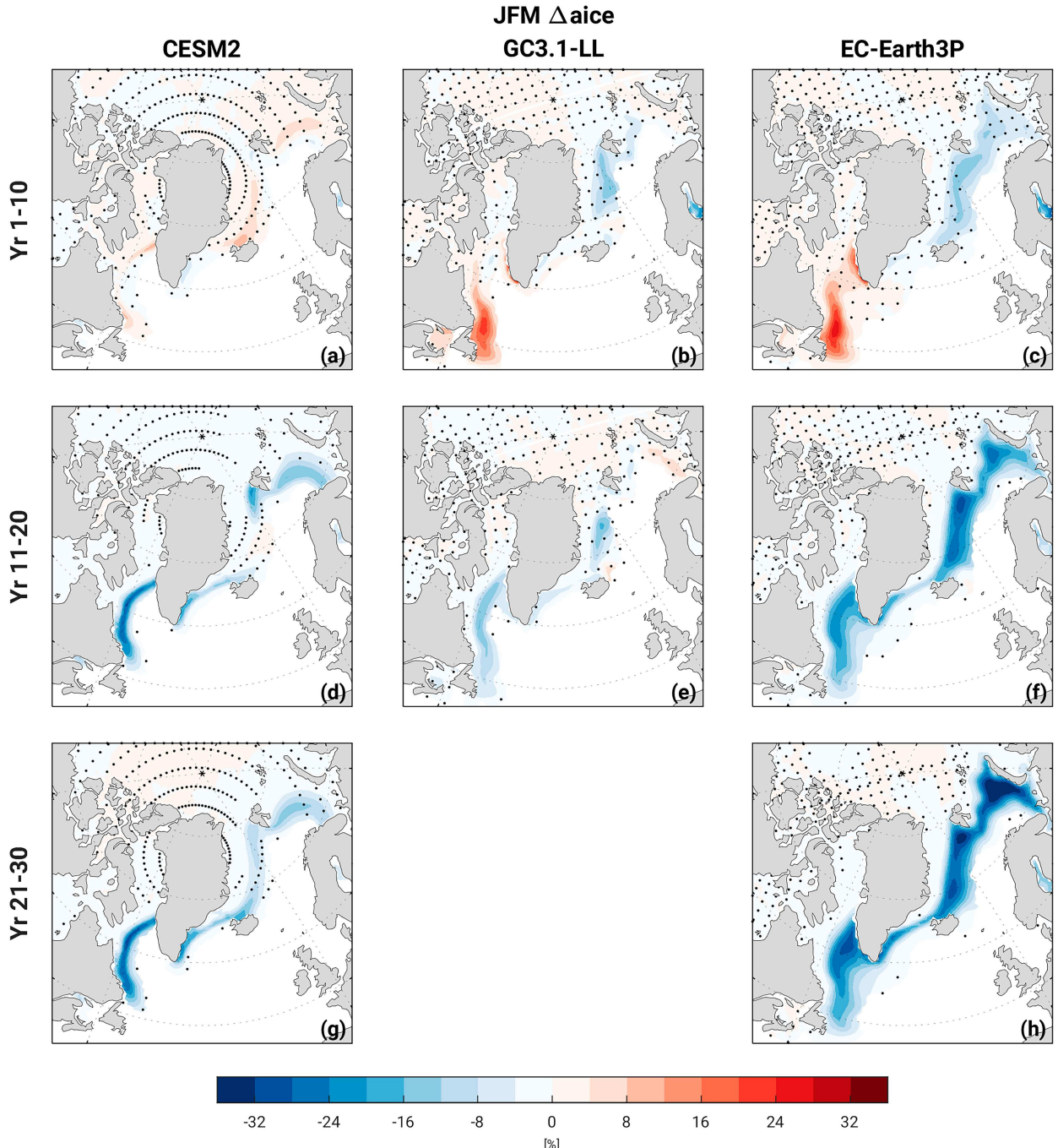


FIG. 11. Difference of JFM sea ice concentration averaged over (a)–(c) years 1–10, (d)–(f) years 11–20, and (g),(h) years 21–30 from (left) CESM2, (center) GC3.1-LL, and (right) EC-Earth3P. The stippled regions indicate that the differences are *not* statistically significant at a 95% confidence level, with every fourth stippling shown.

patterns, however, the magnitude of the responses is substantially different across the models. More precisely, CESM2 shows WMT and AMOC responses roughly twice as large as those in GC3.1-LL and EC-Earth3P, and this is largely because more waters are transformed in the western SPNA in CESM2.

An intriguing finding of the study is that the WMT response directly related to the imposed heat flux forcing is small (Fig. 4) and largely controlled by the expansion and contraction of A_p in response to the forcing and associated exposure of the anomalous A_p to background surface heat fluxes. A schematic of this interaction is illustrated in Fig. 12. We may consider

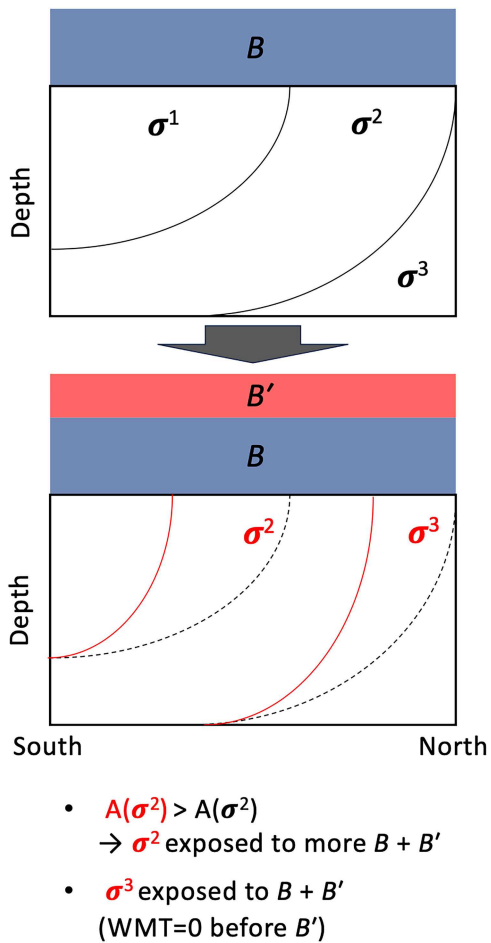


FIG. 12. Schematic summarizing the processes that lead to the WMT response to the imposed forcing in the western SPNA. The black box represents the idealized western SPNA in the depth-latitude plane, and σ^1 , σ^2 , and σ^3 are isopycnal layers under the climatological buoyancy flux (buoyancy loss) B (black) and when the applied buoyancy forcing B' is applied (red). The black dashed lines in the lower box are the same as the initial isopycnals in the upper box. The outcropping area A is the surface integral of the area where isopycnal layers are in contact with the surface.

climatological isopycnal layers (σ^1 and σ^2) that outcrop in the western SPNA under climatological surface buoyancy loss B (upper box in Fig. 12). When forcing B' (additional buoyancy loss) is imposed, the isopycnals move southward, the area of σ^2 becomes wider while the area of σ^1 becomes smaller (lower box in Fig. 12). The wider σ^2 layer is then exposed to B , in addition to B' . In addition, B' can expose an isopycnal layer, σ^3 , to the surface that is not in contact with the surface under B alone. The newly outcropped σ^3 layer is then subjected to surface WMT (which is not under B alone). The enhanced buoyancy loss in σ^2 and σ^3 layers further expands (i.e., larger A_p), thus leading to more exposure to B . Hence, this feedback between outcropping area and background surface buoyancy fluxes enhances WMT much stronger than what B' can directly generate (as $B > B'$). The importance of

A_p for WMT is pointed out by Petit et al. (2021) for subpolar mode water formation in the Iceland Basin from observational estimates, but here we put forward a more nuanced picture by adding on another important factor, feedback from background surface heat fluxes. The background surface heat loss is stronger in CESM2 than in GC3.1-LL and EC-Earth3P in the western SPNA (Fig. 6), thus so does the interaction with A_p . Therefore, the WMT response in the western SPNA is substantially stronger in CESM2.

The stronger background surface heat loss in the western SPNA in CESM2 appears to be closely related to larger warm SST biases than in the other two models (Fig. S12). This suggests that both larger background WMT (Fig. 2) and its response to the NAO heat flux forcing in the western SPNA in CESM2 are likely overestimated. However, while SST biases are relatively small in the western SPNA as well as in the eastern SPNA north of 55°N in GC3.1-LL and EC-Earth3P, sea ice is too extensive relative to satellite observations (Figs. 3d–f). This suggests that the WMT response to the forcing, as well as the background WMT, in these models is possibly underestimated. The importance of surface heat fluxes in WMT highlighted in this study suggests that observational WMT estimates should be sensitive to surface heat flux datasets. Therefore, for a better validation of model performance in WMT, it seems to be important to understand the uncertainty of observational WMT estimates.

Despite the larger AMOC response in CESM2, the amplitude of the SPNA temperature (Fig. 9) and salinity (Fig. S10) responses is comparable across the models. The northward heat and salinity transport anomaly into the SPNA in our experiment is likely due to, to a great extent, the climatological temperature and salinity carried by anomalous velocity as the surface heat flux forcing is only applied north of 45°N. This suggests that the background temperature and salinity in the subtropics are colder and fresher in CESM2 than in GC3.1-LL and EC-Earth3P. The background upper 500-m temperature and salinity in CESM2 are indeed colder and fresher in the subtropics along the Gulf Stream and the NAC (Fig. S13), suggesting that the effect of the larger anomalous velocity is largely compensated by the colder and fresher conditions relative to GC3.1-LL and EC-Earth3P, thus yielding a comparable SPNA temperature and salinity responses as other two models.

A limitation of the present study is the use of low-resolution (1°) ocean models that cannot resolve some important small-scale processes such as mesoscale eddies. Apart from potentially better mean states simulated with a better representation of these processes, high resolution can also have an effect on the response of the ocean to the imposed forcing. For example, eddies shedding from the West Greenland Current have a restratifying effect that inhibits the deep-water formation process in the LS (Tagklis et al. 2020). Thus, the WMT response in the LS, which is the largest contribution to the total WMT response to the forcing in all models, may be weakened if such eddies are resolved. Nevertheless, recent studies comparing decadal WMT and AMOC variability between eddy-rich and non-eddy-resolving models show a consistent, central role of WMT in the LS driving decadal AMOC variability at both resolutions (Oldenburg et al. 2022; Yeager et al. 2021), despite the fact that the high-resolution mean state is in much better

agreement with observations compared to the low-resolution counterpart (i.e., mixed layer depth and overturning strength in the LS; Yeager et al. 2021). While providing insights into the decadal AMOC and SPNA variability in an eddy-rich regime, these studies are all based on CESM1. Thus, it remains to be tested if the same conclusion can be drawn from other high-resolution models.

Finally, although the focus of the present study is the ocean response, we conclude with a brief preview of some of the atmospheric responses that will be more fully examined in a forthcoming study (Fig. S14). These responses are based on the multimodel mean of the ensemble means and the second-decade average (years 11–20) when the SPNA response is largest (Fig. 10). The SPNA warming leads to a warming of surface temperature over most of the Northern Hemisphere land (Fig. S14a). However, compared to the response of up to 1°C warming in the eastern SPNA, the signal is generally very weak over land (<0.3°C). Associated with this summertime warming is a clear northward shift of the tropical rainband in the Atlantic sector that extends farther east to Africa and the Indian Ocean (Fig. S14b). In particular, an increase in precipitation in the Sahel region is evident. The experiment also shows a consistent response of SLP in the subtropical North Atlantic centered around the Iberian Peninsula in boreal winter. This subtropical anomaly is accompanied by an anomaly of opposite sign north of 60°N (Fig. S14c) although the sign of the difference does not agree in all models except over Greenland and Iceland. Together with a negative anomaly south of Alaska, the anomaly pattern suggests a negative Northern Annular Mode (NAM)-like response. We note that all these impacts are generally consistent with those associated with AMOC-driven AMV that can be found in literature (e.g., Zhang et al. 2019) and those identified in Kim et al. (2020) using a similar experiment where NAO heat flux forcing is applied only in the LS.

Acknowledgments. This study is supported by the joint U.K.-NERC/U.S.-NSF WISHBONE project (NE/T013516/1, NSF-2040020). YRR is supported by a “la Caixa” Foundation fellowship (ID 100010434) and the European Union’s Horizon 2020 research and innovation programme under the Marie Skłodowska-Curie Grant Agreement No. 847648. JR is additionally funded by NERC via the SNAP-DRAGON (NE/T013494/1) and CANARI (NE/W004984/1) projects, and via UKRI via the EPOC project. Computing resources (<https://doi.org/10.5065/D6RX99HX>) for CESM2 simulations were provided by the Climate Simulation Laboratory at NCAR’s Computational and Information Systems Laboratory. GC3.1-L1 simulations used Monsoon2, a collaborative High-Performance Computing facility funded by the Met Office and the Natural Environment Research Council, and JASMIN, the UK collaborative data analysis facility. NCAR is a major facility sponsored by NSF under Cooperative Agreement No. 1852977.

Data availability statement. Because of the large size of data, all NAO heat flux forcing experiments from three models will be made available upon request.

REFERENCES

Årthun, M., T. Eldevik, E. Viste, H. Drange, T. Furevik, H. L. Johnson, and N. S. Keenlyside, 2017: Skillful prediction of northern climate provided by the ocean. *Nat. Commun.*, **8**, 15875, <https://doi.org/10.1038/ncomms15875>.

Ba, J., and Coauthors, 2014: A multi-model comparison of Atlantic multidecadal variability. *Climate Dyn.*, **43**, 2333–2348, <https://doi.org/10.1007/s00382-014-2056-1>.

Barrier, N., J. Deshayes, A.-M. Treguier, and C. Cassou, 2015: Heat budget in the North Atlantic subpolar gyre: Impacts of atmospheric weather regimes on the 1995 warming event. *Prog. Oceanogr.*, **130**, 75–90, <https://doi.org/10.1016/j.pocean.2014.10.001>.

Biastoch, A., C. W. Böning, J. Getzlaff, J.-M. Molines, and G. Madec, 2008: Causes of interannual–decadal variability in the meridional overturning circulation of the midlatitude North Atlantic Ocean. *J. Climate*, **21**, 6599–6615, <https://doi.org/10.1175/2008JCLI2404.1>.

Böning, C. W., M. Scheinert, J. Dengg, A. Biastoch, and A. Funk, 2006: Decadal variability of subpolar gyre transport and its reverberation in the North Atlantic overturning. *Geophys. Res. Lett.*, **33**, L21S01, <https://doi.org/10.1029/2006GL026906>.

Borchert, L. F., H. Pohlmann, J. Baehr, N.-C. Neddermann, L. Suarez-Gutierrez, and W. A. Müller, 2019: Decadal predictions of the probability of occurrence for warm summer temperature extremes. *Geophys. Res. Lett.*, **46**, 14 042–14 051, <https://doi.org/10.1029/2019GL085385>.

Chafik, L., S. Häkkinen, M. H. England, J. A. Carton, S. Nigam, A. Ruiz-Barradas, A. Hannachi, and L. Miller, 2016: Global linkages originating from decadal oceanic variability in the subpolar North Atlantic. *Geophys. Res. Lett.*, **43**, 10 909–10 919, <https://doi.org/10.1002/2016GL071134>.

Clement, A., K. Bellomo, L. N. Murphy, M. A. Cane, T. Mauritzen, G. Rädel, and B. Stevens, 2015: The Atlantic multidecadal oscillation without a role for ocean circulation. *Science*, **350**, 320–324, <https://doi.org/10.1126/science.aab3980>.

Comiso, J. C. 2000 (updated 2015): Bootstrap Sea Ice Concentrations from Nimbus-7 SMMR and DMSP SSM/I-SSMIS, version 2. NASA National Snow and Ice Data Center Distributed Active Archive Center, accessed January 2024, <https://doi.org/10.5067/J6JQLS9EJ5HU>.

Danabasoglu, G., and Coauthors, 2016: North Atlantic simulations in Coordinated Ocean-ice Reference Experiments phase II (CORE-II). Part II: Inter-annual to decadal variability. *Ocean Model.*, **97**, 65–90, <https://doi.org/10.1016/j.ocemod.2015.11.007>.

—, and Coauthors, 2020: The Community Earth System Model version 2 (CESM2). *J. Adv. Model. Earth Syst.*, **12**, e2019MS001916, <https://doi.org/10.1029/2019MS001916>.

Delworth, T. L., and F. Zeng, 2016: The impact of the North Atlantic Oscillation on climate through its influence on the Atlantic meridional overturning circulation. *J. Climate*, **29**, 941–962, <https://doi.org/10.1175/JCLI-D-15-0396.1>.

—, —, G. A. Vecchi, X. Yang, L. Zhang, and R. Zhang, 2016: The North Atlantic Oscillation as a driver of rapid climate change in the Northern Hemisphere. *Nat. Geosci.*, **9**, 509–512, <https://doi.org/10.1038/ngeo2738>.

—, —, L. Zhang, R. Zhang, G. A. Vecchi, and X. Yang, 2017: The central role of ocean dynamics in connecting the North Atlantic Oscillation to the extratropical component of

the Atlantic multidecadal oscillation. *J. Climate*, **30**, 3789–3805, <https://doi.org/10.1175/JCLI-D-16-0358.1>.

Deser, C., M. A. Alexander, S.-P. Xie, and A. S. Phillips, 2010: Sea surface temperature variability: Patterns and mechanisms. *Annu. Rev. Mar. Sci.*, **2**, 115–143, <https://doi.org/10.1146/annurev-marine-120408-151453>.

Dunstone, N. J., D. M. Smith, and R. Eade, 2011: Multi-year predictability of the tropical Atlantic atmosphere driven by the high latitude North Atlantic Ocean. *Geophys. Res. Lett.*, **38**, L14701, <https://doi.org/10.1029/2011GL047949>.

Eden, C., and J. Willebrand, 2001: Mechanism of interannual to decadal variability of the North Atlantic circulation. *J. Climate*, **14**, 2266–2280, [https://doi.org/10.1175/1520-0442\(2001\)014<2266:MOITDV>2.0.CO;2](https://doi.org/10.1175/1520-0442(2001)014<2266:MOITDV>2.0.CO;2).

Fasullo, J. T., A. S. Phillips, and C. Deser, 2020: Evaluation of leading modes of climate variability in the CMIP archives. *J. Climate*, **33**, 5527–5545, <https://doi.org/10.1175/JCLI-D-19-1024.1>.

Frankcombe, L. M., A. von der Heydt, and H. A. Dijkstra, 2010: North Atlantic multidecadal climate variability: An investigation of dominant time scales and processes. *J. Climate*, **23**, 3626–3638, <https://doi.org/10.1175/2010JCLI3471.1>.

Grist, J. P., R. Marsh, and S. A. Josey, 2009: On the relationship between the North Atlantic meridional overturning circulation and the surface-forced overturning streamfunction. *J. Climate*, **22**, 4989–5002, <https://doi.org/10.1175/2009JCLI2574.1>.

—, S. A. Josey, R. Marsh, Y.-O. Kwon, R. J. Bingham, and A. T. Blaker, 2014: The surface-forced overturning of the North Atlantic: Estimates from modern era atmospheric reanalysis datasets. *J. Climate*, **27**, 3596–3618, <https://doi.org/10.1175/JCLI-D-13-00070.1>.

Haarsma, R., and Coauthors, 2020: HighResMIP versions of EC-Earth: EC-Earth3P and EC-Earth3P-HR—Description, model computational performance and basic validation. *Geosci. Model Dev.*, **13**, 3507–3527, <https://doi.org/10.5194/gmd-13-3507-2020>.

Hazeleger, W., and R. Bintanja, 2012: Studies with the EC-Earth seamless Earth system prediction model. *Climate Dyn.*, **39**, 2609–2610, <https://doi.org/10.1007/s00382-012-1577-8>.

Hersbach, H., and Coauthors, 2020: The ERA5 global reanalysis. *Quart. J. Roy. Meteor. Soc.*, **146**, 1999–2049, <https://doi.org/10.1002/qj.3803>.

Hurrell, J. W., 1995: Decadal trends in the North Atlantic oscillation: Regional temperatures and precipitation. *Science*, **269**, 676–679, <https://doi.org/10.1126/science.269.5224.676>.

Jackson, L. C., and T. Petit, 2023: North Atlantic overturning and water mass transformation in CMIP6 models. *Climate Dyn.*, **60**, 2871–2891, <https://doi.org/10.1007/s00382-022-06448-1>.

Josey, S. A., J. P. Grist, and R. Marsh, 2009: Estimates of meridional overturning circulation variability in the North Atlantic from surface density flux fields. *J. Geophys. Res.*, **114**, C09022, <https://doi.org/10.1029/2008JC005230>.

—, J. J. M. Hirschi, B. Sinha, A. Duche, J. P. Grist, and R. Marsh, 2018: The recent Atlantic cold anomaly: Causes, consequences, and related phenomena. *Annu. Rev. Mar. Sci.*, **10**, 475–501, <https://doi.org/10.1146/ANNUREV-MARINE-121916-063102>.

Jungclaus, J. H., H. Haak, M. Latif, and U. Mikolajewicz, 2005: Arctic–North Atlantic interactions and multidecadal variability of the meridional overturning circulation. *J. Climate*, **18**, 4013–4031, <https://doi.org/10.1175/JCLI3462.1>.

Kerr, R. A., 2000: A North Atlantic climate pacemaker for the centuries. *Science*, **288**, 1984–1985, <https://doi.org/10.1126/science.288.5473.1984>.

Kim, H.-J., S.-I. An, J.-H. Park, M.-K. Sung, D. Kim, Y. Choi, and J.-S. Kim, 2023: North Atlantic Oscillation impact on the Atlantic meridional overturning circulation shaped by the mean state. *npj Climate Atmos. Sci.*, **6**, 25, <https://doi.org/10.1038/s41612-023-00354-x>.

Kim, W. M., S. Yeager, P. Chang, and G. Danabasoglu, 2016: Atmospheric conditions associated with Labrador Sea deep convection: New insights from a case study of the 2006/07 and 2007/08 winters. *J. Climate*, **29**, 5281–5297, <https://doi.org/10.1175/JCLI-D-15-0527.1>.

—, —, —, and —, 2018a: Low-frequency North Atlantic climate variability in the Community Earth System Model large ensemble. *J. Climate*, **31**, 787–813, <https://doi.org/10.1175/JCLI-D-17-0193.1>.

—, S. G. Yeager, and G. Danabasoglu, 2018b: Key role of internal ocean dynamics in Atlantic multidecadal variability during the last half century. *Geophys. Res. Lett.*, **45**, 13 449–13 457, <https://doi.org/10.1029/2018GL080474>.

—, S. Yeager, and G. Danabasoglu, 2020: Atlantic multidecadal variability and associated climate impacts initiated by ocean thermohaline dynamics. *J. Climate*, **33**, 1317–1334, <https://doi.org/10.1175/JCLI-D-19-0530.1>.

Kirtman, B., and Coauthors, 2013: Near-term climate change: Projections and predictability. *Climate Change 2013: The Physical Science Basis*, T. F. Stocker et al., Eds., Cambridge University Press, 953–1028, https://www.ipcc.ch/site/assets/uploads/2018/02/WG1AR5_Chapter11_FINAL.pdf.

Kuhlbrodt, T., and Coauthors, 2018: The low-resolution version of HadGEM3 GC3.1: Development and evaluation for global climate. *J. Adv. Model. Earth Syst.*, **10**, 2865–2888, <https://doi.org/10.1029/2018MS001370>.

Lai, W. K. M., J. I. Robson, L. J. Wilcox, and N. Dunstone, 2022: Mechanisms of internal Atlantic multidecadal variability in HadGEM3-GC3.1 at two different resolutions. *J. Climate*, **35**, 1365–1383, <https://doi.org/10.1175/JCLI-D-21-0281.1>.

Large, W. G., and S. G. Yeager, 2009: The global climatology of an interannually varying air-sea flux data set. *Climate Dyn.*, **33**, 341–364, <https://doi.org/10.1007/s00382-008-0441-3>.

Lohmann, K., H. Drange, and M. Bentsen, 2009: Response of the North Atlantic subpolar gyre to persistent North Atlantic oscillation like forcing. *Climate Dyn.*, **32**, 273–285, <https://doi.org/10.1007/s00382-008-0467-6>.

MacGilchrist, G. A., H. L. Johnson, C. Lique, and D. P. Marshall, 2021: Demons in the North Atlantic: Variability of deep ocean ventilation. *Geophys. Res. Lett.*, **48**, e2020GL092340, <https://doi.org/10.1029/2020GL092340>.

Mahajan, S., R. Zhang, and T. L. Delworth, 2011: Impact of the Atlantic meridional overturning circulation (AMOC) on Arctic surface air temperature and sea ice variability. *J. Climate*, **24**, 6573–6581, <https://doi.org/10.1175/2011JCLI4002.1>.

Marshall, J., and F. Schott, 1999: Open-ocean convection: Observations, theory, and models. *Rev. Geophys.*, **37** (1), 1–64, <https://doi.org/10.1029/98RG02739>.

McDougall, T. J., D. R. Jackett, D. G. Wright, and R. Feistel, 2003: Accurate and computationally efficient algorithms for potential temperature and density of seawater. *J. Atmos. Oceanic Technol.*, **20**, 730–741, [https://doi.org/10.1175/1520-0426\(2003\)20<730:AACEAF>2.0.CO;2](https://doi.org/10.1175/1520-0426(2003)20<730:AACEAF>2.0.CO;2).

Moat, B. I., and Coauthors, 2019: Insights into decadal North Atlantic sea surface temperature and ocean heat content

variability from an eddy-permitting coupled climate model. *J. Climate*, **32**, 6137–6161, <https://doi.org/10.1175/JCLI-D-18-0709.1>.

—, D. A. Smeed, D. Rayner, W. E. Johns, R. Smith, D. Volkov, M. O. Barninger, and J. Collins, 2023: Atlantic meridional overturning circulation observed by the RAPID-MOCHA-WBTS (RAPID-Meridional Overturning Circulation and Heatflux Array-Western Boundary Time Series) array at 26N from 2004 to 2022 (v2022.1). British Oceanographic Data Centre-Natural Environment Research Council, UK, accessed 16 October 2023, <https://doi.org/10.5285/04c79ece-3186-349a-e063-6c86abc0158c>.

Oldenburg, D., R. C. J. Wills, K. C. Armour, and L. Thompson, 2022: Resolution dependence of atmosphere–ocean interactions and water mass transformation in the North Atlantic. *J. Geophys. Res. Oceans*, **127**, e2021JC018102, <https://doi.org/10.1029/2021JC018102>.

Oltmanns, M., J. Karstensen, G. W. K. Moore, and S. A. Josey, 2020: Rapid cooling and increased storminess triggered by freshwater in the North Atlantic. *Geophys. Res. Lett.*, **47**, e2020GL087207, <https://doi.org/10.1029/2020GL087207>.

O'Reilly, C. H., M. Huber, T. Woollings, and L. Zanna, 2016: The signature of low-frequency oceanic forcing in the Atlantic multidecadal oscillation. *Geophys. Res. Lett.*, **43**, 2810–2818, <https://doi.org/10.1002/2016GL067925>.

Petit, T., M. S. Lozier, S. A. Josey, and S. A. Cunningham, 2021: Role of air–sea fluxes and ocean surface density in the production of deep waters in the eastern subpolar gyre of the North Atlantic. *Ocean Sci.*, **17**, 1353–1365, <https://doi.org/10.5194/os-17-1353-2021>.

Polo, I., J. Robson, R. Sutton, and M. A. Balmaseda, 2014: The importance of wind and buoyancy forcing for the boundary density variations and the geostrophic component of the AMOC at 26°N. *J. Phys. Oceanogr.*, **44**, 2387–2408, <https://doi.org/10.1175/JPO-D-13-0264.1>.

Qasmi, S., E. Sanchez-Gomez, Y. Ruprich-Robert, J. Boé, and C. Cassou, 2021: Modulation of the occurrence of heatwaves over the Euro-Mediterranean region by the intensity of the Atlantic multidecadal variability. *J. Climate*, **34**, 1099–1114, <https://doi.org/10.1175/JCLI-D-19-0982.1>.

Rhein, M., R. Steinfeldt, D. Kieke, I. Stendardo, and I. Yashayaev, 2017: Ventilation variability of Labrador Sea water and its impact on oxygen and anthropogenic carbon: A review. *Philos. Trans. Roy. Soc.*, **375A**, 20160321, <https://doi.org/10.1098/rsta.2016.0321>.

Robson, J., R. Sutton, K. Lohmann, D. Smith, and M. D. Palmer, 2012: Causes of the rapid warming of the North Atlantic Ocean in the mid-1990s. *J. Climate*, **25**, 4116–4134, <https://doi.org/10.1175/JCLI-D-11-00443.1>.

—, —, and D. Smith, 2014: Decadal predictions of the cooling and freshening of the North Atlantic in the 1960s and the role of ocean circulation. *Climate Dyn.*, **42**, 2353–2365, <https://doi.org/10.1007/s00382-014-2115-7>.

—, P. Ortega, and R. Sutton, 2016: A reversal of climatic trends in the North Atlantic since 2005. *Nat. Geosci.*, **9**, 513–517, <https://doi.org/10.1038/ngeo2727>.

—, I. Polo, D. L. R. Hodson, D. P. Stevens, and L. C. Shaffrey, 2018: Decadal prediction of the North Atlantic subpolar gyre in the HiGEM high-resolution climate model. *Climate Dyn.*, **50**, 921–937, <https://doi.org/10.1007/s00382-017-3649-2>.

Scaife, A. A., and Coauthors, 2019: Does increased atmospheric resolution improve seasonal climate predictions? *Atmos. Sci. Lett.*, **20**, e922, <https://doi.org/10.1002/asl.922>.

Simpson, I. R., C. Deser, K. A. McKinnon, and E. A. Barnes, 2018: Modeled and observed multidecadal variability in the North Atlantic jet stream and its connection to sea surface temperatures. *J. Climate*, **31**, 8313–8338, <https://doi.org/10.1175/JCLI-D-18-0168.1>.

—, S. G. Yeager, K. A. McKinnon, and C. Deser, 2019: Decadal predictability of late winter precipitation in Western Europe through an ocean–jet stream connection. *Nat. Geosci.*, **12**, 613–619, <https://doi.org/10.1038/s41561-019-0391-x>.

Smith, D. M., R. Eade, N. J. Dunstone, D. Fereday, J. M. Murphy, H. Pohlmann, and A. A. Scaife, 2010: Skilful multi-year predictions of Atlantic hurricane frequency. *Nat. Geosci.*, **3**, 846–849, <https://doi.org/10.1038/ngeo1004>.

—, and Coauthors, 2019: Robust skill of decadal climate predictions. *npj Climate Atmos. Sci.*, **2**, 13, <https://doi.org/10.1038/s41612-019-0071-y>.

Speer, K., and E. Tziperman, 1992: Rates of water mass formation in the North Atlantic Ocean. *J. Phys. Oceanogr.*, **22**, 93–104, [https://doi.org/10.1175/1520-0485\(1992\)022<0093:ROWMFI>2.0.CO;2](https://doi.org/10.1175/1520-0485(1992)022<0093:ROWMFI>2.0.CO;2).

Taglialatela, F., A. Bracco, T. Ito, and R. M. Castelao, 2020: Submesoscale modulation of deep water formation in the Labrador Sea. *Sci. Rep.*, **10**, 17489, <https://doi.org/10.1038/s41598-020-74345-w>.

Visbeck, M., E. P. Chassignet, R. G. Curry, T. L. Delworth, R. R. Dickson, and G. Krahmann, 2003: The ocean's response to North Atlantic Oscillation variability. *The North Atlantic Oscillation: Climatic Significance and Environmental Impact*, *Geophys. Monogr.*, Vol. 134, Amer. Geophys. Union, 113–145, <https://doi.org/10.1029/134GM06>.

Walin, G., 1982: On the relation between sea-surface heat flow and thermal circulation in the ocean. *Tellus*, **34**, 187–195, <https://doi.org/10.3402/tellusa.v34i2.10801>.

Wang, X., J. Li, C. Sun, and T. Liu, 2017: NAO and its relationship with the Northern Hemisphere mean surface temperature in CMIP5 simulations. *J. Geophys. Res. Atmos.*, **122**, 4202–4227, <https://doi.org/10.1002/2016JD025979>.

Welch, B. L., 1947: The generalisation of ‘Student’s’ problems when several different population variances are involved. *Biometrika*, **34**, 28–35, <https://doi.org/10.2307/2332510>.

Xu, X., E. P. Chassignet, and F. Wang, 2019: On the variability of the Atlantic meridional overturning circulation transports in coupled CMIP5 simulations. *Climate Dyn.*, **52**, 6511–6531, <https://doi.org/10.1007/s00382-018-4529-0>.

Yeager, S., 2020: The abyssal origins of North Atlantic decadal predictability. *Climate Dyn.*, **55**, 2253–2271, <https://doi.org/10.1007/s00382-020-05382-4>.

—, and G. Danabasoglu, 2014: The origins of late-twentieth-century variations in the large-scale North Atlantic circulation. *J. Climate*, **27**, 3222–3247, <https://doi.org/10.1175/JCLI-D-13-00125.1>.

—, and J. I. Robson, 2017: Recent progress in understanding and predicting Atlantic decadal climate variability. *Curr. Climate Change Rep.*, **3**, 112–127, <https://doi.org/10.1007/s40641-017-0064-z>.

—, A. R. Karspeck, and G. Danabasoglu, 2015: Predicted slowdown in the rate of Atlantic sea ice loss. *Geophys. Res. Lett.*, **42**, 10 704–10 713, <https://doi.org/10.1002/2015GL065364>.

—, and Coauthors, 2021: An outsized role for the Labrador Sea in the multi-decadal variability of the Atlantic overturning circulation. *Sci. Adv.*, **7**, eabh3592, <https://doi.org/10.1126/sciadv.abh3592>.

Zhang, R., 2008: Coherent surface-subsurface fingerprint of the Atlantic meridional overturning circulation. *Geophys. Res. Lett.*, **35**, L20705, <https://doi.org/10.1029/2008GL035463>.

—, R. Sutton, G. Danabasoglu, T. L. Delworth, W. M. Kim, J. Robson, and S. G. Yeager, 2016: Comment on “The Atlantic multidecadal oscillation without a role for ocean circulation”. *Science*, **352**, 1527, <https://doi.org/10.1126/science.aaf1660>.

—, —, —, Y.-O. Kwon, R. Marsh, S. G. Yeager, D. E. Amrhein, and C. M. Little, 2019: A review of the role of the Atlantic meridional overturning circulation in Atlantic multidecadal variability and associated climate impacts. *Rev. Geophys.*, **57**, 316–375, <https://doi.org/10.1029/2019RG000644>.